

# Towards Efficient MPPI Trajectory Generation with Unscented Guidance: U-MPPI Control Strategy

Ihab S. Mohamed<sup>1</sup>, Junhong Xu<sup>1</sup>, Gaurav S Sukhatme<sup>2</sup>, and Lantao Liu<sup>1</sup>

**Abstract**—The classical Model Predictive Path Integral (MPPI) control framework lacks reliable safety guarantees since it relies on a *risk-neutral* trajectory evaluation technique, which can present challenges for safety-critical applications such as autonomous driving. Additionally, if the majority of MPPI sampled trajectories concentrate in high-cost regions, it may generate an *infeasible* control sequence. To address this challenge, we propose the U-MPPI control strategy, a novel methodology that can effectively manage system uncertainties while integrating a more efficient trajectory sampling strategy. The core concept is to leverage the Unscented Transform (UT) to propagate not only the mean but also the covariance of the system dynamics, going beyond the traditional MPPI method. As a result, it introduces a novel and more efficient trajectory sampling strategy, significantly enhancing state-space exploration and ultimately reducing the risk of being trapped in local minima. Furthermore, by leveraging the uncertainty information provided by UT, we incorporate a *risk-sensitive* cost function that explicitly accounts for risk or uncertainty throughout the trajectory evaluation process, resulting in a more resilient control system capable of handling uncertain conditions. By conducting extensive simulations of 2D aggressive autonomous navigation in both known and unknown cluttered environments, we verify the efficiency and robustness of our proposed U-MPPI control strategy compared to the baseline MPPI. We further validate the practicality of U-MPPI through real-world demonstrations in unknown cluttered environments, showcasing its superior ability to incorporate both the UT and local costmap into the optimization problem without introducing additional complexity.

**Index Terms**—Autonomous vehicle navigation, MPPI, unscented transform, occupancy grid map path planning.

## SUPPLEMENTARY MATERIAL

A video showcasing both the simulation and real-world results, including the behavior of the vanilla MPPI, is provided in the supplementary video: <https://youtu.be/1xsh4Bxlrg>. Moreover, the GPU implementation of our proposed U-MPPI algorithm is available at: <https://github.com/IhabMohamed/U-MPPI>.

## I. INTRODUCTION

**P**LANNING and controlling autonomous vehicles under uncertainty is a partially-solved yet highly challenging problem in robotics. The uncertainty or risk can arise from multiple sources, such as the vehicle’s dynamics, the dynamics of other objects in the environment, the presence of unexpected obstacles, and the accuracy of the sensors used to perceive the

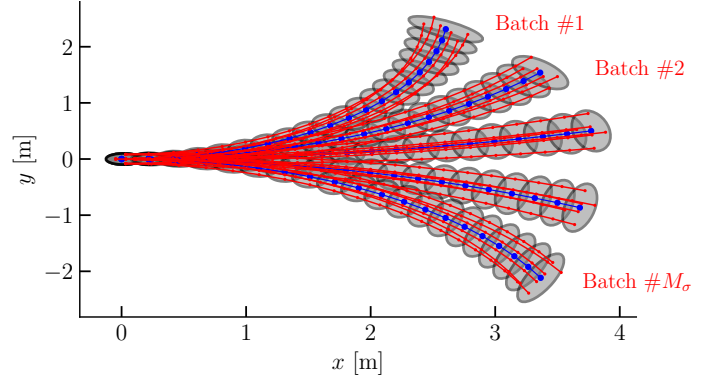


Fig. 1: Our proposed sampling strategy, for a ground vehicle model, under the U-MPPI control strategy based on unscented transform; such a sampling strategy propagates both the mean  $\bar{x}_k$  (blue dots) and covariance  $\Sigma_k$  (gray ellipses) of the state vector at each time-step  $k$ ; to generate  $M$  sampled trajectories, we propagate  $M_\sigma$  sets of batches, where each batch contains  $n_\sigma$  trajectories corresponding to the  $n_\sigma$  sigma points, where  $M = n_\sigma M_\sigma$ ,  $n_\sigma = 2n_x + 1$ , and red lines refer to  $2n_x$  sigma-point trajectories surrounding the nominal trajectories (blue lines); for our validation-used robot,  $n_x = 3$ .

environment. These factors can lead to unpredictable vehicle behavior, making it challenging to anticipate its movements and actions. Therefore, it is crucial for motion planning and control algorithms to account for the uncertainties of the system’s states, sensing, and control actions. This eventually enables autonomous vehicles to adapt to unexpected environmental changes and make reliable decisions in real-time [1].

Model Predictive Control (MPC), also referred to as *receding-horizon* optimal control, has been introduced as an effective solution for improving system safety and managing random disturbances and uncertainties, owing to its flexibility and ability to handle system constraints and nonlinearities while optimizing system performance. It plans a sequence of optimal control inputs over a finite time-horizon by repeatedly solving the optimal control problem using the *receding-horizon* principle, with the first control input applied to the system. There are two main categories of MPC frameworks that can handle various forms of uncertainty: Robust MPC (RMPC) and Stochastic MPC (SMPC). RMPC considers worst-case scenarios of uncertainty to ensure stability and constraint satisfaction, while SMPC takes into account expected costs and probabilistic constraints (e.g., chance constraints) to optimize performance under uncertain conditions. RMPC is known to generate the safest solutions among MPC categories due to its incorporation of worst-case scenarios into the optimization problem and its emphasis on minimizing worst-case objective functions. However, it may lead to excessively conservative control actions, resulting in low system performance [2], [3].

<sup>1</sup>Ihab S. Mohamed, Junhong Xu, and Lantao Liu (corresponding author) are with the Luddy School of Informatics, Computing, and Engineering, Indiana University, Bloomington, IN 47408 USA (e-mail: {mohamedi, xu14, lantao}@iu.edu)

<sup>2</sup>Gaurav S Sukhatme is with the Department of Computer Science, University of Southern California, Los Angeles, CA 90089, USA (e-mail: gaurav@usc.edu)

On the other hand, despite the superior ability of SMPC to leverage the probabilistic nature of uncertainties, many SMPC approaches have performance limitations, including being tailored to specific forms of stochastic noise, requiring dynamics linearization to ensure a *real-time* performance and implementation of the control strategy, and employing chance constraints that may not accurately reflect the severity of constraint violations or potential accidents and can be computationally demanding to evaluate, particularly for complex or high-dimensional probability distributions [4], [5]. Additionally, SMPC has a further limitation in that it relies on a *risk-neutral* expectation to predict future uncertain outcomes, which may not be reliable in the case of a tail-end probability event (i.e., a rare event with a low probability of occurring) actually happening [6]. To address the challenges posed by uncertainties, Risk-Sensitive MPC (RSMPC) approaches have gained traction in recent years, thanks to their ability to balance the benefits and drawbacks of robust and stochastic MPC methods. By integrating the concept of *risk measures* or *risk metrics* into the optimization problem, RSMPC can evaluate the impact of uncertainty and adjust responses accordingly to different levels of uncertainty [7]–[9].

The Model Predictive Path Integral (MPPI) framework, a type of SMPC method, has emerged as a promising control strategy for complex robotics systems with stochastic dynamics and uncertainties [10]–[13]. Such a method solves the stochastic optimal control problem in a *receding-horizon* control setting by: (i) leveraging Monte Carlo simulation to rollout real-time simulated trajectories propagated from the system dynamics, (ii) evaluating these trajectories, (iii) computing the optimal control sequence by taking the weighted average of the costs of the sampled trajectories, and (iv) applying the first control input to the system while using the remaining control sequence to warm-start the optimization in the next time-step, enabling the method to solve the optimization problem effectively [11]. MPPI stands out among alternative MPC methods due to its attractive features, such as being a sampling-based and derivative-free optimization method, not relying on assumptions or approximations of objective functions and system dynamics, being effective for highly dynamic systems, and benefiting from parallel sampling and the computational capabilities of Graphics Processing Units (GPUs) to achieve optimized and *real-time* performance [14]<sup>1</sup>.

While MPPI has appealing characteristics, it may also pose challenges in practice. One particular concern is that, much like any sampling-based optimization algorithm, it could generate an *infeasible* control sequence if all the resulting MPPI sampled trajectories are concentrated in a high-cost region, which may lead to violations of system constraints or a higher likelihood of being trapped in local minima [15], [16]. In [17], Tube-MPPI was proposed as a solution to alleviate the situation by incorporating an iterative Linear Quadratic Gaussian (iLQG) controller (which, unfortunately, requires the linearization of dynamics) as an ancillary controller to track the MPPI-generated nominal trajectory. Similarly, in

[13], an augmented version of MPPI is employed, which includes a nonlinear  $\mathcal{L}_1$  adaptive controller to address model uncertainty. Recently, novel sampling techniques have been introduced to enhance the performance of MPPI, as discussed in [15] and [16]. In [15], the MPPI algorithm is enhanced by incorporating the covariance steering (CS) principle, while [16] proposes sampling trajectories from a product of normal and log-normal distributions (NLN mixture), instead of solely using a Gaussian distribution. These methods result in more efficient trajectories than the vanilla MPPI, leading to better exploration of the system’s state-space and reducing the risk of encountering local minima.

Another constraint of MPPI is its inability to explicitly incorporate risk levels during planning due to its *risk-neutral* technique in evaluating sampled trajectories during the optimization process, making it challenging to achieve the desired balance between risk and robustness. Additionally, the MPPI optimization problem concentrates solely on minimizing the objective function, which is influenced by a minor perturbation injected into the control input, without explicitly considering any uncertainties or risks associated with the system dynamics or the environment. This can eventually lead to sub-optimal or overly aggressive control actions, as MPPI may select trajectories that appear to have a low expected cost but may actually be riskier or less robust in practice. Consequently, MPPI cannot guarantee safety when environmental conditions change, which limits its applicability for safety-critical applications such as autonomous driving. The Risk-aware MPPI (RA-MPPI) algorithm [18] is a more recent approach that addresses this issue by utilizing Conditional Value-at-Risk (CVaR) to generate risk-averse controls that evaluate real-time risks and account for systematic uncertainties. However, such a method employs Monte-Carlo sampling to estimate the CVaR, which can be computationally intensive and time-consuming since generating a large number of random samples is required for accurate estimation using Monte Carlo methods.

In contrast to existing solutions aimed at mitigating the shortcomings of MPPI, our proposed solution can effectively reflect the uncertainties of system states, sensing, and control actions, in addition to integrating a novel and more efficient trajectory sampling strategy. To this end, we introduce the U-MPPI control strategy, a novel methodology that enhances the classical MPPI algorithm by combining the Unscented Transform (UT) with standard optimal control theory (also known as unscented guidance [19]) to effectively manage system uncertainties. Such a control strategy leverages the UT for two purposes: regulating the propagation of the dynamical system and proposing a new state-dependent cost function formulation that incorporates uncertainty information. To the best of the authors’ knowledge, the proposed control strategy has not been previously discussed in the literature. In summary, the contributions of this work can be summarized as follows:

- 1) While vanilla MPPI variants propagate only the mean value of the system dynamics, as depicted in Fig. 2, we propose a novel trajectory sampling technique equipped with a more effective sampling distribution policy based on UT; this technique utilizes UT to propagate both the mean and covariance of the system dynamics at each

<sup>1</sup>It is worth noting that a CPU-based MPPI, optimized using vectorization and tensor operations, is now available. See the link for further information: <https://github.com/artofnothingness/mppi>

time-step, as demonstrated in Figs. 1 and 3, and explained in detail in Section IV-A; by doing so, our new sampling method achieves significantly better exploration of the state-space of the given system and reduces the risk of getting trapped in local minima.

- 2) Then, by utilizing the propagated uncertainty information (i.e., state covariance matrix), we introduce a *risk-sensitive* cost function that explicitly considers risk or uncertainty during the trajectory evaluation process, leading to a safer and more robust control system, especially for safety-critical applications, as discussed in Section IV-B.
- 3) In Sections V and VI, we validate the effectiveness of our U-MPPI control strategy for aggressive collision-free navigation in both known and unknown cluttered environments using both intensive simulations and real-world experiments; by comparing it with the baseline MPPI, we demonstrate its superiority in producing more efficient trajectories that explore the state-space of the system better, resulting in higher success and task completion rates, reducing the risk of getting trapped in local minima, and ultimately leading the robot to find feasible trajectories that avoid collisions.

## II. STOCHASTIC OPTIMAL CONTROL

This section aims to establish the problem statement of stochastic optimal control and present a concise overview of MPPI as a potential solution to address this problem.

### A. Problem Formulation

Within the context of discrete-time stochastic systems, let us consider the system state  $\mathbf{x}_k \in \mathbb{R}^{n_x}$ , the control input  $\mathbf{u}_k \in \mathbb{R}^{n_u}$ , and the underlying non-linear dynamics

$$\mathbf{x}_{k+1} = f(\mathbf{x}_k, \mathbf{w}_k). \quad (1)$$

The actual (i.e., disturbed) control input,  $\mathbf{w}_k$ , is represented as  $\mathbf{w}_k = \mathbf{u}_k + \delta\mathbf{u}_k \sim \mathcal{N}(\mathbf{u}_k, \Sigma_{\mathbf{u}})$ , where  $\delta\mathbf{u}_k \sim \mathcal{N}(\mathbf{0}, \Sigma_{\mathbf{u}})$  is a zero-mean Gaussian noise with covariance  $\Sigma_{\mathbf{u}}$  which represents the injected disturbance into the control input. Within a finite time-horizon  $N$ , we denote the control sequence  $\mathbf{U} = [\mathbf{u}_0, \mathbf{u}_1, \dots, \mathbf{u}_{N-1}]^\top \in \mathbb{R}^{n_u N}$  and the corresponding state trajectory  $\mathbf{x} = [\mathbf{x}_0, \mathbf{x}_1, \dots, \mathbf{x}_N]^\top \in \mathbb{R}^{n_x(N+1)}$ . Moreover, let  $\mathcal{X}^d$  denote the  $d$  dimensional space with  $\mathcal{X}_{rob}(\mathbf{x}_k) \subset \mathcal{X}^d$  and  $\mathcal{X}_{obs} \subset \mathcal{X}^d$  represent the area occupied by the robot and obstacles, respectively. In this scenario, the objective of the stochastic optimal control problem is to find the optimal control sequence,  $\mathbf{U}$ , that generates a collision-free trajectory, guiding the robot from its initial state,  $\mathbf{x}_s$ , to the desired state,  $\mathbf{x}_f$ , under the minimization of the cost function,  $J$ , subject to specified constraints. The optimization problem at hand can be formulated using the vanilla MPPI control strategy as

$$\min_{\mathbf{U}} J(\mathbf{x}, \mathbf{u}) = \mathbb{E} \left[ \phi(\mathbf{x}_N) + \sum_{k=0}^{N-1} \left( q(\mathbf{x}_k) + \frac{1}{2} \mathbf{u}_k^\top R \mathbf{u}_k \right) \right], \quad (2a)$$

$$\text{s.t. } \mathbf{x}_{k+1} = f(\mathbf{x}_k, \mathbf{w}_k), \delta\mathbf{u}_k \sim \mathcal{N}(\mathbf{0}, \Sigma_{\mathbf{u}}), \quad (2b)$$

$$\mathcal{X}_{rob}(\mathbf{x}_k) \cap \mathcal{X}_{obs} = \emptyset, h(\mathbf{x}_k, \mathbf{u}_k) \leq 0, \quad (2c)$$

$$\mathbf{x}_0 = \mathbf{x}_s, \mathbf{u}_k \in \mathbb{U}, \mathbf{x}_k \in \mathbb{X}, \quad (2d)$$

where  $R \in \mathbb{R}^{n_u \times n_u}$  is a positive-definite control weighting matrix,  $\mathbb{U}$  denotes the set of admissible control inputs, and  $\mathbb{X}$  denotes the set of all possible states  $\mathbf{x}_k$ ; the state terminal cost function,  $\phi(\mathbf{x}_N)$ , and the running cost function,  $q(\mathbf{x}_k)$ , can be defined as arbitrary functions, offering a more flexible and dynamic approach to cost modeling that can be adapted to meet the specific requirements of the system being controlled.

### B. Overview of MPPI Control Strategy

MPPI solves the optimization problem defined in (2) by minimizing the objective function  $J$  (2a), taking into account the system dynamics (2b) and constraints, including collision avoidance and control constraints, detailed in (2c). To this end, at each time-step  $\Delta t$ , MPPI employs the Monte Carlo simulation to sample thousands of *real-time* simulated trajectories, represented by  $M$ , propagated from the underlying system dynamics, as illustrated in Fig. 2. Subsequently, within the

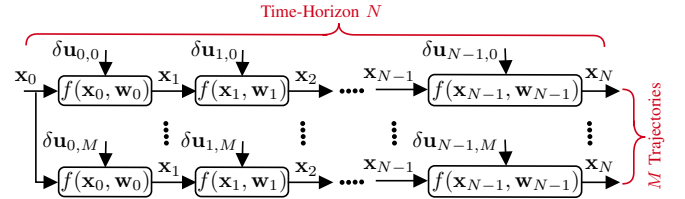


Fig. 2: Schematic illustration of system dynamics propagation in MPPI for  $M$  sampled trajectories over a finite time-horizon  $N$ .

time-horizon  $N$ , the *cost-to-go* of each trajectory  $\tau_i$  can be evaluated as

$$\tilde{S}(\tau_i) = \phi(\mathbf{x}_N) + \sum_{k=0}^{N-1} \tilde{q}(\mathbf{x}_k, \mathbf{u}_k, \delta\mathbf{u}_{k,i}), \forall i \in \{1, \dots, M\}, \quad (3)$$

where  $\phi(\mathbf{x}_N)$  refer to the terminal state cost, while the instantaneous running cost  $\tilde{q}(\mathbf{x}_k, \mathbf{u}_k, \delta\mathbf{u}_k)$  encompasses both the state-dependent running cost  $q(\mathbf{x}_k)$  and the quadratic control cost  $q(\mathbf{u}_k, \delta\mathbf{u}_k)$  and is formulated as

$$\tilde{q} = \underbrace{q(\mathbf{x}_k)}_{\text{State-dep.}} + \underbrace{\gamma_{\mathbf{u}} \delta\mathbf{u}_{k,i}^\top R \delta\mathbf{u}_{k,i} + \mathbf{u}_k^\top R \delta\mathbf{u}_{k,i} + \frac{1}{2} \mathbf{u}_k^\top R \mathbf{u}_k}_{q(\mathbf{u}_k, \delta\mathbf{u}_k): \text{Quadratic Control Cost}}, \quad (4)$$

where  $\gamma_{\mathbf{u}} = \frac{\nu-1}{2\nu}$ , and  $\nu \in \mathbb{R}^+$  determines the level of aggressiveness in exploring the state-space.

As stated in [11], the vanilla MPPI algorithm updates the optimal control sequence  $\{\mathbf{u}_k\}_{k=0}^{N-1}$  by considering a weighted average cost from all of the simulated trajectories; mathematically, this control sequence can be expressed as

$$\mathbf{u}_k \leftarrow \mathbf{u}_k + \frac{\sum_{m=1}^M \exp\left(\frac{-1}{\lambda} [\tilde{S}(\tau_m) - \tilde{S}_{\min}]\right) \delta\mathbf{u}_{k,m}}{\sum_{m=1}^M \exp\left(\frac{-1}{\lambda} [\tilde{S}(\tau_m) - \tilde{S}_{\min}]\right)}, \quad (5)$$

which incorporates the *cost-to-go* of the  $m^{\text{th}}$  trajectory  $\tilde{S}(\tau_m)$ , the minimum cost trajectory among all simulated rollouts  $\tilde{S}_{\min}$  that prevents numerical overflow or underflow, without affecting the optimality of the algorithm, and the inverse temperature  $\lambda$  that governs the selectiveness of the weighted average of trajectories. The resulting sequence is then smoothed with

a Savitzky-Galoy filter [20], followed by applying the first control  $\mathbf{u}_0$  to the system, while the remaining sequence is utilized for warm-starting the next optimization step.

### III. UNSCENTED OPTIMAL CONTROL

In this section, we present a comprehensive overview of the unscented transform, followed by the unscented guidance technique, which combines the unscented transform with standard stochastic optimal control theory to generate a robust *open-loop* method for managing system uncertainties.

#### A. Unscented Transform

The unscented transform (UT), proposed by Julier and Uhlmann [21], aims to create nonlinear filters without the need for linearization. It approximates a probability distribution function (PDF) after it passes through a non-linear transformation using a set of sampled points, known as sigma points [22].

Formally, given the mean  $\bar{\mathbf{x}}_k$  and covariance  $\Sigma_k$  of a Gaussian-distributed system state  $\mathbf{x}_k$ , with  $\mathbf{x}_k \sim \mathcal{N}(\bar{\mathbf{x}}_k, \Sigma_k)$ , UT approximates the distribution over the next state,  $\mathbf{x}_{k+1}$ , by first introducing a set of sigma points  $\{\mathcal{X}_k^{(i)}\}_{i=0}^{2n_x} \in \mathbb{R}^{n_x}$  around the mean  $\bar{\mathbf{x}}_k$  and the corresponding weights  $\{w^{(i)}\}_{i=0}^{2n_x} \in \mathbb{R}^{2n_x}$ , where  $n_\sigma = 2n_x + 1$ . These sigma points are designed to capture the covariance of the distribution at time-step  $k$  as follows

$$\begin{aligned} \mathcal{X}_k^{(0)} &= \bar{\mathbf{x}}_k, \\ \mathcal{X}_k^{(i)} &= \bar{\mathbf{x}}_k + \left( \sqrt{(n_x + \lambda_\sigma) \Sigma_k} \right)_i, \quad \forall i = \{1, \dots, n_x\}, \\ \mathcal{X}_k^{(i)} &= \bar{\mathbf{x}}_k - \left( \sqrt{(n_x + \lambda_\sigma) \Sigma_k} \right)_i, \quad \forall i = \{n_x + 1, \dots, 2n_x\}, \end{aligned} \quad (6)$$

where  $\left( \sqrt{(n_x + \lambda_\sigma) \Sigma_k} \right)_i$  represents the  $i^{\text{th}}$  row or column of the square root of the weighted covariance matrix  $(n_x + \lambda_\sigma) \Sigma_k$ , and  $\lambda_\sigma = \alpha^2(n_x + k_\sigma) - n_x$  is influenced by the scaling parameters  $k_\sigma \geq 0$  and  $\alpha \in (0, 1]$  that determine how far the sigma points are spread from the mean [23], as demonstrated in Fig. 4. Each  $\mathcal{X}_k^{(i)}$  is associated with two weights,  $w_m^{(i)}$  for computing the mean and  $w_c^{(i)}$  for determining the covariance of the transformed distribution, computed as

$$\begin{aligned} w_m^{(0)} &= \frac{\lambda_\sigma}{n_x + \lambda_\sigma}, \\ w_c^{(0)} &= w_m^{(0)} + (1 - \alpha^2 + \beta), \\ w_m^{(i)} &= w_c^{(i)} = \frac{1}{2(n_x + \lambda_\sigma)}, \end{aligned} \quad (7)$$

where  $\beta$  is a hyper-parameter controlling the relative importance of the mean and covariance information. In other words,  $\beta$  is employed to incorporate prior knowledge about the distribution of the state  $\mathbf{x}$ . For Gaussian distributions, the optimal value for  $\beta$  is 2 [24]. In the second step, we propagate the  $(2n_x + 1)$  sigma points through the non-linear system to produce the transformed sigma points  $\mathcal{X}_{k+1}^{(i)} = f(\mathcal{X}_k^{(i)})$  at the next time-step. Finally, the mean and covariance of  $\mathbf{x}_{k+1}$

can be estimated using the transformed sigma points and their corresponding weights, as follows

$$\begin{aligned} \bar{\mathbf{x}}_{k+1} &= \sum_{i=0}^{2n_x} w_m^{(i)} \mathcal{X}_{k+1}^{(i)}, \\ \Sigma_{k+1} &= \sum_{i=0}^{2n_x} w_c^{(i)} (\mathcal{X}_{k+1}^{(i)} - \bar{\mathbf{x}}_{k+1})(\mathcal{X}_{k+1}^{(i)} - \bar{\mathbf{x}}_{k+1})^\top. \end{aligned} \quad (8)$$

#### B. Unscented Optimal Control

By incorporating the unscented transform with standard optimal control, the unscented optimal control, also referred to as unscented guidance [19], presents a novel methodology for addressing the uncertainties in non-linear dynamical systems within an *open-loop* framework [25], [26]. Given the sigma points  $\mathcal{X}_k^{(i)}$  and disturbed control input  $\mathbf{w}_k$  at time-step  $k$ , each sigma point can be propagated through the underlying non-linear dynamics given in (1), as follows

$$\mathcal{X}_{k+1}^{(i)} = f\left(\mathcal{X}_k^{(i)}, \mathbf{w}_k\right), \quad \forall i = 0, \dots, 2n_x \in \mathbb{R}^{n_\sigma}. \quad (9)$$

Consider an  $n_\sigma n_x$ -dimensional vector  $\mathbf{X}$ , defined as  $\mathbf{X} = [\mathcal{X}^{(0)}, \mathcal{X}^{(1)}, \dots, \mathcal{X}^{(2n_x)}]^\top \in \mathbb{R}^{n_\sigma n_x}$ . Then, the dynamics of  $\mathbf{X}$  are characterized by  $n_\sigma$  instances of the function  $f$ , specified as

$$\mathbf{X}_{k+1} = \begin{bmatrix} f\left(\mathcal{X}_k^{(0)}, \mathbf{w}_k\right) \\ f\left(\mathcal{X}_k^{(1)}, \mathbf{w}_k\right) \\ \vdots \\ f\left(\mathcal{X}_k^{(2n_x)}, \mathbf{w}_k\right) \end{bmatrix} := \mathbf{f}(\mathbf{X}_k, \mathbf{w}_k). \quad (10)$$

With these preliminaries, the original stochastic optimal control problem described in (2) can be re-formulated within the context of the unscented guidance framework as

$$\min_{\mathbf{U}} \mathbf{J}(\mathbf{X}, \mathbf{u}) = \mathbb{E} \left[ \Phi(\mathbf{X}_N) + \sum_{k=0}^{N-1} \left( \mathbf{q}(\mathbf{X}_k) + \frac{1}{2} \mathbf{u}_k^\top \mathbf{R} \mathbf{u}_k \right) \right], \quad (11a)$$

$$\text{s.t. } \mathbf{X}_{k+1} = \mathbf{f}(\mathbf{X}_k, \mathbf{w}_k), \delta \mathbf{u}_k \sim \mathcal{N}(\mathbf{0}, \Sigma_{\mathbf{u}}), \quad (11b)$$

$$\mathcal{X}_{\text{rob}}(\mathbf{X}_k) \cap \mathcal{X}_{\text{obs}} = \emptyset, \mathbf{h}(\mathbf{X}_k, \mathbf{u}_k) \leq 0, \quad (11c)$$

$$\mathbf{X}_0 = [\mathcal{X}_0^{(0)}, \dots, \mathcal{X}_0^{(2n_x)}]^\top, \mathbf{u}_k \in \mathbb{U}, \mathbf{X}_k \in \mathbb{X}, \quad (11d)$$

where  $\Phi(\mathbf{X}_N) = [\phi(\mathcal{X}_N^{(0)}), \dots, \phi(\mathcal{X}_N^{(2n_x)})]^\top \in \mathbb{R}^{n_\sigma}$ , and  $\mathbf{q}(\mathbf{X}_k) = [q(\mathcal{X}_k^{(0)}), \dots, q(\mathcal{X}_k^{(2n_x)})]^\top \in \mathbb{R}^{n_\sigma}$ . The objective of our proposed U-MPPI control strategy, as detailed in Section IV, is to minimize the objective function,  $\mathbf{J}$ , in (11a) by finding the optimal control sequence,  $\mathbf{U} = \{\mathbf{u}_k\}_{k=0}^{N-1}$ , while taking into account (i) the system constraints previously discussed in Section II-A, and (ii) the uncertainties associated with both system states and control actions.

### IV. U-MPPI CONTROL STRATEGY

As previously outlined in Section II-B, the control noise variance  $\Sigma_{\mathbf{u}}$  is not updated by MPPI, and the state-space exploration is performed by adjusting  $\nu$  (refer to (4)). Nevertheless, a too-high value of  $\nu$  can cause control inputs with

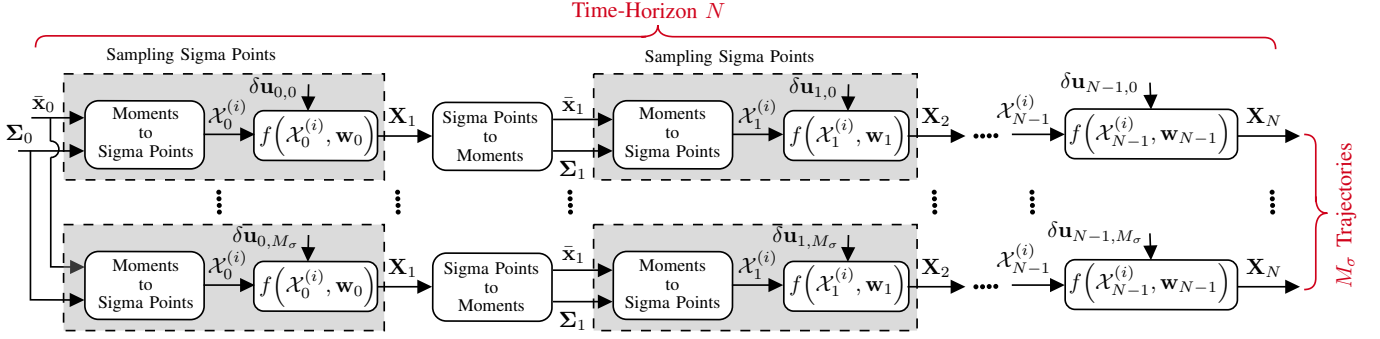


Fig. 3: Schematic illustration of nonlinear dynamical system propagation under the proposed U-MPPI control strategy for  $M$  sampled trajectories over a finite time-horizon  $N$ , where  $M = n_\sigma M_\sigma$ .

considerable chatter. Similarly, increasing  $\Sigma_{\mathbf{u}}$  might violate system constraints and eventual divergence from the desired state [16]. Additionally, the MPPI problem, as stated in (2), is focused solely on minimizing the cost function that is affected by a minor perturbation in the control input, represented by  $\delta \mathbf{u}_k$ , without explicitly incorporating the uncertainties that may be associated with either the system states or the surrounding environment. To ensure effectiveness in practice, the motion control strategy should be able to reflect the uncertainties of system states, sensing, and control actions. To this end, we introduce the U-MPPI control strategy, a new technique that leverages unscented transform to deal with these uncertainties. More precisely, the Unscented Transform (UT) is utilized for the purpose of regulating the propagation of the dynamical system, thereby introducing a novel and more efficient trajectory sampling strategy than the standard MPPI variants, as demonstrated in Section IV-A. Furthermore, as discussed in Section IV-B, UT proposes a new cost function formulation incorporating uncertainty information, leading to a safer and more robust control system, especially for safety-critical applications.

#### A. Unscented-Based Sampling Strategy

By leveraging Monte Carlo simulation, the vanilla MPPI algorithm simulates a large number of *real-time* trajectories  $M$ , propagated from the system dynamics defined in (1), by solely manipulating the injected Gaussian noise into the mean control sequence (see Fig. 2). Additionally, the computation of the propagated states during the time period of  $N$  is restricted to the mean value or the first moment with respect to the initial state  $\mathbf{x}_0$ , without propagating the covariance of  $\mathbf{x}_k$ . Therefore, to enhance the performance of the classic MPPI algorithm, we propose a new trajectory sampling technique that utilizes the Unscented Transform (UT) to propagate both the mean  $\bar{\mathbf{x}}_k$  and covariance  $\Sigma_k$  of the state vector  $\mathbf{x}_k$  at each time-step  $k$ .

In Fig. 3, we illustrate how the sigma points propagate through the nonlinear dynamical system within the U-MPPI control framework, leading to a total of  $M$  rollouts. These rollouts are achieved by sampling  $M_\sigma$  sets of batches, also referred to as cones, with each batch comprising  $n_\sigma$  trajectories, such that  $M = n_\sigma M_\sigma$ . The propagation process of our proposed sampling strategy can be summarized in the following steps. At time-step  $k = 0$ , we compute  $n_\sigma$  sigma points

$\{\mathcal{X}_0^{(i)}\}_{i=0}^{2n_x}$  using (6), given the initial state  $\mathbf{x}_0 \sim \mathcal{N}(\bar{\mathbf{x}}_0, \Sigma_0)$ . We then apply the underlying non-linear dynamics expressed in (9) to the sigma points, which can be merged into a single vector using (10). Finally, we use the resulting sigma points  $\mathbf{X}_1$  at  $k = 1$  to estimate the first and second moments, namely  $\bar{\mathbf{x}}_1$  and  $\Sigma_1$ , of the propagated state vector  $\mathbf{x}_1$  by applying (8). This propagation process is repeated until  $k = N - 1$ , resulting in a sequence of state vectors denoted as  $\{\mathbf{X}_k\}_{k=0}^N$ , which represent the  $n_\sigma$  propagated sigma points. This entire process is carried out for each batch, resulting in a total of  $M$  trajectories. In this study, during time-step  $k$ , we assume that all sigma points belonging to the  $m^{\text{th}}$  batch are being affected by the same Gaussian control noise represented by  $\delta \mathbf{u}_{k,m}$ . Figure 1 depicts the visual representation of our proposed unscented-based sampling strategy displayed in Fig. 3.

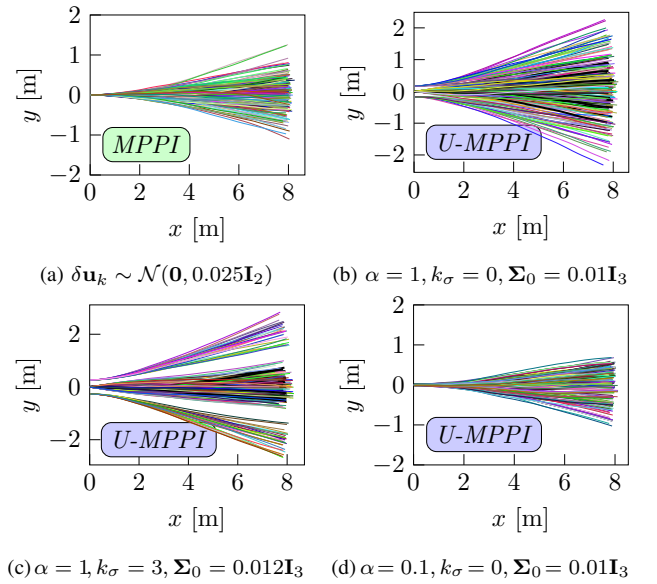


Fig. 4: Distribution of 210 sampled trajectories generated by (a) MPPI with  $\delta \mathbf{u}_k \sim \mathcal{N}(\mathbf{0}, 0.025\mathbf{I}_2)$  and (b) U-MPPI with the same perturbation in the control input  $\delta \mathbf{u}_k$  but with different UT parameters; in both methods, the robot is assumed to be initially located at  $\mathbf{x} = [x, y, \theta]^T = [0, 0, 0]^T$  in ([m], [m], [deg]), with a commanded control input  $\mathbf{u} = [v, \omega]^T = [1, 0]^T$  in ([m/s], [rad/s]).

The primary objective of the new sampling strategy is to achieve significantly better exploration of the state-space of the given system and more efficient sampling of trajectories

compared to MPPI, while utilizing the same injected control noise  $\Sigma_u$ . To exemplify how leveraging the UT for trajectory sampling can enhance the performance of the MPPI algorithm and to investigate the effect of UT parameters on the distribution of sampled rollouts, we present a concrete example in Fig. 4. In particular, using the discrete-time kinematics model of a differential wheeled robot from [16] and control schemes parameters listed in Section V-A1, we generate 210 rollouts by sampling  $\delta \mathbf{u}_k$  from a zero-mean Gaussian distribution with a covariance of  $0.025\mathbf{I}_2$  under the classical MPPI framework, as illustrated in Fig. 4(a), where  $\mathbf{I}_n$  denotes an  $n \times n$  identity matrix. Similarly, we employ the unscented-based sampling strategy to draw 210 trajectories, considering: (i) the same injected disturbance into the control input, i.e.,  $\delta \mathbf{u}_k \sim \mathcal{N}(\mathbf{0}, 0.025\mathbf{I}_2)$ , and (ii) setting the UT scaling parameters to  $\alpha = 1$  and  $k_\sigma = 0$ , along with an initial state covariance matrix  $\Sigma_0$  of  $0.01\mathbf{I}_3$ , as illustrated in Fig. 4(b). It is noteworthy to observe in Fig. 4(b) that our proposed sampling strategy is more efficient than the classical MPPI sampling strategy, as it generates more spread-out trajectories that cover a larger state space. This enables the robot to explore the environment more extensively and find better solutions, thereby reducing the likelihood of getting trapped in local minima, as revealed in Section V-A4. Nevertheless, as depicted in Fig. 4(c), employing higher values of UT parameters (specifically,  $\alpha, k_\sigma, \Sigma_0$ ) may result in a loss of precision and continuity in the distribution of trajectories across the state-space, as the sigma points become more spread out from the mean  $\mathcal{X}_k^{(0)}$ . This can impact the resulting control actions of the system and, in the context of autonomous navigation, potentially lead to collisions with obstacles. In contrast, Fig. 4(d) demonstrates that using lower values of  $\alpha$  and  $k_\sigma$  results in a sampling strategy that closely resembles MPPI. Similarly, if trajectories are sampled only from  $\mathcal{X}_k^{(0)}$  (as depicted by the blue trajectories in Fig. 1), while excluding other sigma-point trajectories, the same sampling strategy can be achieved. We refer to this approach as sampling mode 0 ( $SM_0$ ), while the default strategy that includes all sigma points is referred to as  $SM_1$ .

## B. Risk-Sensitive Cost

One of the main limitations of the vanilla MPPI is that it typically assumes a *risk-neutral* approach when assessing the sampled trajectories during the optimization process, without explicitly considering risk or uncertainty in the trajectory evaluation process, as outlined in Section II-B, particularly in (4). The commonly employed method in sampling-based MPC algorithms involves using a quadratic cost function to guide the current state  $\mathbf{x}_k$  towards its desired state  $\mathbf{x}_f$ , denoted as  $q_{\text{state}}(\mathbf{x}_k)$ , and expressed mathematically as follows

$$q_{\text{state}}(\mathbf{x}_k) = (\mathbf{x}_k - \mathbf{x}_f)^\top \mathbf{Q} (\mathbf{x}_k - \mathbf{x}_f) = \|\mathbf{x}_k - \mathbf{x}_f\|_{\mathbf{Q}}^2, \quad (12)$$

where  $\mathbf{Q}$  is a positive definite weighting matrix. Whittle introduced in [27] an interesting method for incorporating risk in decision-making by replacing the expected quadratic cost with a risk-sensitive benchmark in the form of an exponential-quadratic function. The *risk-sensitive* (RS) cost  $q_{\text{rs}}(\mathbf{x}_k)$  can be

obtained by evaluating the log-expectation of the exponentiated quadratic cost as follows

$$\begin{aligned} q_{\text{rs}}(\mathbf{x}_k) &= -\frac{2}{\gamma} \log \mathbb{E} \left[ \exp \left( -\frac{1}{2} \gamma q_{\text{state}}(\mathbf{x}_k) \right) \right] \\ &= -\frac{2}{\gamma} \log \mathbb{E} \left[ \exp \left( -\frac{1}{2} \gamma \|\mathbf{x}_k - \mathbf{x}_f\|_{\mathbf{Q}}^2 \right) \right], \end{aligned} \quad (13)$$

where  $\gamma$  is a real scalar denoted as the *risk-sensitivity* parameter, dictating how the controller reacts to risk or uncertainty. For example, when  $\gamma > 0$ , the controller exhibits *risk-seeking* or *risk-preferring* behavior. Conversely, when  $\gamma < 0$ , the controller demonstrates *risk-averse* or *risk-avoiding* behavior. When  $\gamma = 0$ , the controller is considered *risk-neutral*. We refer to [7] for more details and clear visualizations demonstrating the relationship between the sign of  $\gamma$  and the RS cost  $q_{\text{rs}}$ .

Our proposed U-MPPI control strategy assumes that the system state  $\mathbf{x}_k \sim \mathcal{N}(\bar{\mathbf{x}}_k, \Sigma_k)$  follows Gaussian distribution. With this assumption, we can approximate the RS state-dependent cost expressed in (13) as

$$q_{\text{rs}}(\mathbf{x}_k) = \frac{1}{\gamma} \log \det (\mathbf{I} + \gamma \mathbf{Q} \Sigma_k) + \|\bar{\mathbf{x}}_k - \mathbf{x}_f\|_{Q_{\text{rs}}}^2, \quad (14)$$

where  $Q_{\text{rs}}$  represents the *risk-sensitive* penalty coefficients matrix or adaptive weighting matrix, given by  $Q_{\text{rs}}(\Sigma_k) = (\mathbf{Q}^{-1} + \gamma \Sigma_k)^{-1}$ . The derivation of (14) is given in Appendix A. Such a new formulation is employed by U-MPPI to assess each batch of sigma-point trajectories, where the predicted mean state  $\bar{\mathbf{x}}_k$  is replaced with the predicted sigma points  $\{\mathcal{X}_k^{(i)}\}_{i=0}^{2n_x}$ . Therefore, the modified RS cost for the  $i^{\text{th}}$  U-MPPI sampled trajectory within a certain batch is defined by

$$q_{\text{rs}}(\mathcal{X}_k^{(i)}, \Sigma_k) = \frac{1}{\gamma} \log \det (\mathbf{I} + \gamma \mathbf{Q} \Sigma_k) + \|\mathcal{X}_k^{(i)} - \mathbf{x}_f\|_{Q_{\text{rs}}}^2. \quad (15)$$

It is noteworthy to observe in (15) that  $q_{\text{rs}}(\cdot)$  incorporates uncertainty information  $\Sigma_k$  as a feedback into the weighting matrix  $\mathbf{Q}$ , which measures the difference between the predicted sigma point  $\mathcal{X}_k^{(i)}$  and the desired state  $\mathbf{x}_f$ . By incorporating this uncertainty feedback mechanism, the proposed control strategy exhibits a risk-sensitive behavior that effectively minimizes the RS cost over the time-horizon  $N$ . This, in turn, enables the development of a more robust and risk-conscious control policy, as empirically validated through intensive simulations outlined in Section V. To be more precise, if  $\gamma < 0$ , the penalty coefficients matrix  $Q_{\text{rs}}$  utilized for tracking the desired state increases with the level of system uncertainty  $\Sigma_k$ . This can be expressed mathematically over a finite time-horizon  $N$  as  $Q_{\text{rs}}(\Sigma_0) < Q_{\text{rs}}(\Sigma_1) < \dots < Q_{\text{rs}}(\Sigma_{N-1})$  for all  $\gamma < 0$ . On the other hand, if  $\gamma > 0$ , the penalty matrix decreases as the uncertainty level increases. Additionally, when  $\gamma = 0$ , the penalty remains constant and equal to the weighting matrix  $\mathbf{Q}$ , regardless of the level of the uncertainty [8]. More in-depth analysis of how the U-MPPI performance is influenced by the sign of  $\gamma$  is discussed in Section V-A1.

By incorporating the system uncertainty  $\Sigma_k$  into (3), we can obtain the modified *cost-to-go* for each trajectory  $\tau_m^{(i)}$  in batch  $m$  as

$$\begin{aligned} \tilde{S}(\tau_m^{(i)}) &= \phi(\mathcal{X}_N^{(i)}) + \sum_{k=0}^{N-1} \tilde{q}(\mathcal{X}_k^{(i)}, \Sigma_k, \mathbf{u}_k, \delta \mathbf{u}_{k,m}), \\ \forall m \in \{1, \dots, M_\sigma\}, \quad \forall i \in \{0, \dots, 2n_x\}, \end{aligned} \quad (16)$$

where the instantaneous running cost  $\tilde{q}$  is a combination of the state-dependent running cost  $q(\mathcal{X}_k^{(i)}, \Sigma_k)$ , which relies on the RS cost defined in (15) (as shown in (18) as an example), as well as the quadratic control cost  $q(\mathbf{u}_k, \delta \mathbf{u}_k)$  from (4). Note that the *cost-to-go* for all sigma-point trajectories in the  $m^{\text{th}}$  batch can be expressed in vector form as  $\tilde{\mathbf{S}}(\tau_m) = [\tilde{S}(\tau_m^{(0)}), \dots, \tilde{S}(\tau_m^{(2n_x)})]^\top \in \mathbb{R}^{n_\sigma}$ . Similarly,  $\tilde{\mathbf{q}}(\mathbf{X}_k, \Sigma_k, \mathbf{u}_k, \delta \mathbf{u}_{k,m}) = [\tilde{q}(\mathcal{X}_k^{(0)}, \cdot), \dots, \tilde{q}(\mathcal{X}_k^{(2n_x)}, \cdot)]^\top$ .

---

**Algorithm 1** Real-Time U-MPPI Control Algorithm

---

**Given:**

$M, M_\sigma, N$ : # of trajectories, batches, time-horizon,  
 $\mathbf{f}, n_x, \Delta t$ : Dynamics, state dimension, time-step size,  
 $\phi, q, Q, \gamma, \lambda, \nu, \Sigma_{\mathbf{u}}, R$ : Cost/Control parameters,  
 $\lambda_\sigma, k_\sigma, n_\sigma, \alpha, \beta, \Sigma_0$ : UT parameters,  
 SGF: Savitzky-Galoy (SG) convolutional filter,

**Input:**

$\mathbf{U} = [\mathbf{u}_0, \mathbf{u}_1, \dots, \mathbf{u}_{N-1}]^\top$ : Initial control sequence,  
 SM: Set U-MPPI sampling mode (SM<sub>0</sub> OR SM<sub>1</sub>),

```

1: while task not completed do
2:    $\bar{\mathbf{x}}_0 \leftarrow \text{StateEstimator}()$ ,  $\triangleright \bar{\mathbf{x}}_0 \in \mathbb{R}^{n_x}$ 
3:    $\delta \mathbf{u} \leftarrow \text{RandomNoiseGenerator}(\mathbf{0}, \Sigma_{\mathbf{u}})$ ,  $\triangleright \delta \mathbf{u} \in \mathbb{R}^{N \times M_\sigma}$ 
4:   for  $m \leftarrow 1$  to  $M_\sigma$  in parallel do
5:      $(\bar{\mathbf{x}}, \Sigma) \leftarrow (\bar{\mathbf{x}}_0, \Sigma_0)$ ,  $\triangleright \text{Actual state } \mathbf{x}_0 \sim \mathcal{N}(\bar{\mathbf{x}}_0, \Sigma_0)$ 
6:      $\tilde{\mathbf{S}}(\tau_m) \leftarrow [0, \dots, 0]^\top$ ,  $\triangleright \tilde{\mathbf{S}}(\tau_m) \in \mathbb{R}^{n_\sigma}$ 
7:     for  $k \leftarrow 0$  to  $N - 1$  do
8:        $\mathbf{X}_k \leftarrow \text{Moments2SigmaPoints}(\bar{\mathbf{x}}_k, \Sigma_k)$ ,
9:        $\mathbf{X}_{k+1} \leftarrow \mathbf{X}_k + \mathbf{f}(\mathbf{X}_k, \mathbf{u}_k + \delta \mathbf{u}_{k,m}) \Delta t$ ,
10:       $\tilde{\mathbf{S}}(\tau_m) \leftarrow \tilde{\mathbf{S}}(\tau_m) + \tilde{\mathbf{q}}(\mathbf{X}_k, \Sigma_k, \mathbf{u}_k, \delta \mathbf{u}_{k,m})$ ,
11:       $(\bar{\mathbf{x}}_{k+1}, \Sigma_{k+1}) \leftarrow \text{SigmaPoints2Moments}(\mathbf{X}_{k+1})$ ,
12:    end for
13:     $\tilde{\mathbf{S}}(\tau_m) \leftarrow \tilde{\mathbf{S}}(\tau_m) + \Phi(\mathbf{X}_N)$ ,
14:  end for
15:   $\tilde{S}_{\min} \leftarrow \min_m [\tilde{\mathbf{S}}(\tau_m)]$ ,  $\forall m = \{1, \dots, M_\sigma\}$ 
16:  for  $k \leftarrow 0$  to  $N - 1$  do
17:     $\mathbf{u}_k \leftarrow \text{SGF}\left(\mathbf{u}_k + \frac{\sum_{m=0}^{M_\sigma} \exp\left(\frac{-1}{\lambda} [\tilde{\mathbf{S}}(\tau_m) - \tilde{S}_{\min}] \right) \delta \mathbf{u}_{k,m}}{\sum_{m=0}^{M_\sigma} \exp\left(\frac{-1}{\lambda} [\tilde{\mathbf{S}}(\tau_m) - \tilde{S}_{\min}] \right)}\right)$ ,
18:  end for
19:   $\mathbf{u}_0 \leftarrow \text{SendToActuators}(\mathbf{U})$ ,
20:  for  $k \leftarrow 1$  to  $N - 1$  do
21:     $\mathbf{u}_{k-1} \leftarrow \mathbf{u}_k$ ,
22:  end for
23:   $\mathbf{u}_{N-1} \leftarrow \text{ControlSequenceInitializer}(\mathbf{u}_{N-1})$ ,
24:  Check for task completion
25: end while

```

---

**C. Real-Time U-MPPI Control Algorithm**

We are now prepared to describe the *real-time* control-loop of our U-MPPI algorithm, as depicted in Algorithm 1, employing the default sampling strategy that considers all sigma points (referred to as SM<sub>1</sub>). At every time-step  $\Delta t$ , the algorithm estimates the current system state  $\bar{\mathbf{x}}_0$  with an external state estimator, generates  $N \times M_\sigma$  random control perturbations  $\delta \mathbf{u}$  on the GPU using CUDA's random number generation library, and then produces  $M_\sigma$  sets of batches

in parallel on the GPU (lines 2 : 4). Subsequently, for each batch and starting from the actual (i.e., initial) state  $\mathbf{x}_0 \sim \mathcal{N}(\bar{\mathbf{x}}_0, \Sigma_0)$ , the algorithm samples and propagates  $n_\sigma$  sigma-point trajectories by applying the non-linear dynamics in (10) to the sigma points computed via (6) (lines 5 : 9). These trajectories are then evaluated using (16), and the first and second moments of the propagated state are estimated by applying (8) (lines 10 : 15). Then, the algorithm updates the optimal control sequence  $\{\mathbf{u}_k\}_{k=0}^{N-1}$ , applies a Savitzky-Galoy filter for smoothing, and applies the first control  $\mathbf{u}_0$  to the system (lines 16 : 19). It then slides down the remaining sequence of length  $N - 1$  to be utilized at the next time-step (lines 20 : 23). It is noteworthy that when executing the algorithm in sampling mode 0 (SM<sub>0</sub>), where only the mean  $\mathcal{X}_k^{(0)}$  is used for trajectory sampling, it is essential to set  $M_\sigma$  to  $M$  instead of  $\text{int}(\frac{M}{n_\sigma})$ . Additionally, it is necessary to evaluate solely the *cost-to-go* of the nominal trajectory  $\tilde{S}(\tau_m^{(0)})$ .

**V. SIMULATION-BASED EVALUATION**

In this section, we evaluate the effectiveness of our proposed control strategy by comparing it to the standard MPPI control framework. Herein, we focus on two goal-oriented autonomous ground vehicle (AGV) navigation tasks in 2D cluttered environments. The first task, presented in Section V-A, involves maneuvering the AGV within a given map. This experiment allows us to understand the algorithmic advantages of the proposed U-MPPI control scheme without adding real-world complexity. Section V-B introduces a more complex and realistic scenario where the map is unknown a priori. It examines the adaptability and robustness of our proposed control strategy, providing a thorough evaluation of its potential in real-world applications.

**A. Aggressive Navigation in Known Cluttered Environments**

*1) Simulation Setup:* In this experiment, we use the kinematics model of a differential drive robot presented in [16] for sampling trajectories in the conventional MPPI and propagating sigma points in the proposed U-MPPI technique, as outlined in (9). The model's state includes its position and orientation in the world frame  $\mathcal{F}_o$ , given by  $\mathbf{x} = [x, y, \theta]^\top \in \mathbb{R}^3$ . The control input consists of the robot's desired linear and angular velocities, denoted by  $\mathbf{u} = [v, \omega]^\top \in \mathbb{R}^2$ .

To ensure a fair comparison, both MPPI and U-MPPI simulations were conducted under consistent parameters. A time prediction of 8s and a control rate of 30Hz were employed, resulting in 240 control time-steps (i.e.,  $N = 240$ ). At each time-step  $\Delta t$ , a total of 2499 rollouts were sampled, accompanied by an exploration noise of  $\nu = 1200$ . To account for control weighting, a control weighting matrix  $R$  was utilized, which was formulated as  $\lambda \Sigma_{\mathbf{u}}^{-\frac{1}{2}}$ . Additionally, the inverse temperature parameter was set to  $\lambda = 0.572$ , while the control noise variance matrix  $\Sigma_{\mathbf{u}} = \text{Diag}(\sigma_v^2, \sigma_\omega^2)$  was defined as  $\Sigma_{\mathbf{u}} = \text{Diag}(0.023, 0.028)$ . To smooth the control sequence, we utilized the Savitzky-Galoy (SG) convolutional filter with a quintic polynomial function, i.e.,  $n_{sg} = 5$ , and a window length  $l_{sg}$  of 61. As described in Section IV-A, U-MPPI has additional parameters in the unscented transform to

regulate the spread of the sigma points. These parameters are set to  $\alpha = 1$ ,  $k_\sigma = 0.5$ , and  $\beta = 2$ . Additionally, the initial state covariance matrix  $\Sigma_0$  is set to  $0.001\mathbf{I}_3$ . The baseline and U-MPPI are implemented using Python and incorporated within the Robot Operating System (ROS) framework. They are executed in *real-time* on an NVIDIA GeForce GTX 1660 Ti laptop GPU.

In the context of the 2D navigation task, MPPI employs a commonly-used instantaneous state-dependent cost function described in (17). This cost function consists of two terms. The first term, denoted as  $q_{\text{state}}(\mathbf{x}_k)$ , encourages the robot to reach the desired state; its formulation, which employs a quadratic expression, is provided in (12). The second term,  $q_{\text{crash}}(\mathbf{x}_k) = w_{\text{crash}}\mathbb{I}_{\text{crash}}$ , serves as an indicator function that imposes a high penalty when the robot collides with obstacles, with  $\mathbb{I}_{\text{crash}}$  being a Boolean variable and  $w_{\text{crash}}$  representing the collision weighting coefficient. While implementing the proposed U-MPPI approach, we replace the quadratic cost  $q_{\text{state}}(\mathbf{x}_k)$ , as depicted in (18), with our newly introduced RS cost denoted as  $q_{\text{rs}}(\mathcal{X}_k^{(i)}, \Sigma_k)$  and defined in (15). Within the scope of this work, we set the values of  $Q$  and  $w_{\text{crash}}$  as follows:  $Q = \text{Diag}(2.5, 2.5, 2)$  and  $w_{\text{crash}} = 10^3$ . It is worth noting that in this particular task, assigning positive values to  $\gamma$  (i.e.,  $\gamma > 0$ ) ensures a trade-off between compelling the robot to reach its desired state and minimizing the risk of collisions with obstacles. This trade-off arises from the fact that the penalty coefficients matrix  $Q_{\text{rs}}$ , utilized for tracking the desired state, decreases as the system uncertainty  $\Sigma_k$  increases over the time-horizon  $N$ . Therefore, we have chosen  $\gamma = 1$  to maintain this trade-off and strike a balance between task completion and collision avoidance. On the other hand, we believe that assigning negative values to  $\gamma$  in applications such as autonomous racing [28] and visual servoing [14] could enhance the performance of U-MPPI. In such tasks, it is crucial to prioritize forcing the current state to reach its desired state, which can be achieved by assigning a higher penalty coefficients matrix  $Q_{\text{rs}}$ .

$$q(\mathbf{x}_k) = q_{\text{state}}(\mathbf{x}_k) + q_{\text{crash}}(\mathbf{x}_k). \quad (17)$$

$$q(\mathcal{X}_k^{(i)}, \Sigma_k) = q_{\text{rs}}(\mathcal{X}_k^{(i)}, \Sigma_k) + q_{\text{crash}}(\mathbf{x}_k). \quad (18)$$

2) *Simulation Scenario*: In order to assess the effectiveness of the proposed control framework within cluttered environments, three distinct scenarios with different difficulty levels were examined. In each scenario, we randomly generate one unique forest type consisting of 25 individual forests, resulting in a total of  $\mathcal{N}_T = 25$  tasks. Each forest represents a cluttered environment with dimensions of  $50\text{ m} \times 50\text{ m}$ . In the first scenario (referred to as *Scenario #1*), the average distance between obstacles was 1.5 m, indicated as  $d_{\text{min}}^{\text{obs}} = 1.5\text{ m}$ ; while in the second and third scenarios (i.e., *Scenario #2* and *Scenario #3*), they were placed at average distances of 2 m and 3 m, respectively. Additionally, we set the maximum desired velocity  $v_{\text{max}}$  of the robot based on the degree of clutter in each scenario. Specifically,  $v_{\text{max}}$  is set to 2 m/s, 3 m/s, and 4 m/s in *Scenario #1*, *#2*, and *#3*, respectively.

3) *Performance Metrics*: To achieve a fair comparison between the two control strategies, we use the following criteria: (i) firstly, in all simulation instances, the robot is required to reach the designated desired pose, denoted as  $\mathbf{x}_f = [50, 50, 0]^\top$ , from a predetermined initial pose  $\mathbf{x}_0 = [0, 0, 0]^\top$ , measured in ([m], [m], [deg]); (ii) secondly, a comprehensive set of metrics are defined to evaluate the overall performance [16], including the *task completion percentage*  $\mathcal{T}_c$ , the *success rate*  $\mathcal{S}_R$ , the *average number of collisions*  $\mathcal{N}_c$ , the *average number of local minima occurrences*  $\mathcal{R}_{\text{lm}}$ , the *average distance traversed by the robot*  $d_{\text{av}}$  to reach the desired state  $\mathbf{x}_f$  from its initial state  $\mathbf{x}_0$ , the *average linear velocity*  $v_{\text{av}}$  of the robot during the execution of its task in the cluttered environment, and the *average execution time per iteration*  $t_{\text{exec}}$  of the control algorithm. Successful task completion is characterized by the robot reaching the desired pose without colliding with obstacles within a predefined finite time, i.e.,  $\mathcal{T}_c = 100\%$ ,  $\mathcal{N}_c = 0$ , and  $\mathcal{R}_{\text{lm}} = 0$ . Furthermore, in all the given scenarios, if the robot fails to reach the desired pose within a duration of 70 s while successfully avoiding collisions with obstacles, we classify the simulation episode as reaching a local minimum, indicated by  $\mathcal{R}_{\text{lm}} = 1$ .

TABLE I: Performance comparisons of the two control schemes, where the gray cells represent better results.

Scheme	$\mathcal{R}_{\text{lm}}(\mathcal{N}_c)$	$\mathcal{S}_R$ [%]	$\mathcal{T}_c$ [%]	$d_{\text{av}}$ [m]	$v_{\text{av}}$ [m/s]	$t_{\text{exec}}$ [ms]
<b>Scenario #1:</b> $v_{\text{max}} = 2\text{ m/s}$ & $d_{\text{min}}^{\text{obs}} = 1.5\text{ m}$ , $\gamma = 1$ , $w_{\text{crash}} = 10^3$						
MPPI	9 (2)	78	92.86	75.18	$1.84 \pm 0.18$	9.68
U-MPPI	2 (0)	96	98.78	75.34	$1.85 \pm 0.17$	9.12
<b>Scenario #2:</b> $v_{\text{max}} = 3\text{ m/s}$ & $d_{\text{min}}^{\text{obs}} = 2\text{ m}$ , $\gamma = 1$ , $w_{\text{crash}} = 10^3$						
MPPI	2 (1)	94	98	75.31	$2.49 \pm 0.73$	10.03
U-MPPI	0 (0)	100	100	75.78	$2.53 \pm 0.49$	8.87
<b>Scenario #3:</b> $v_{\text{max}} = 4\text{ m/s}$ & $d_{\text{min}}^{\text{obs}} = 3\text{ m}$ , $\gamma = 1$ , $w_{\text{crash}} = 10^3$						
MPPI	0 (0)	100	100	72.19	$3.51 \pm 0.74$	8.55
U-MPPI	0 (0)	100	100	71.98	$3.54 \pm 0.59$	7.7

4) *Simulation Results*: Table I presents the performance analysis of the proposed U-MPPI and the baseline MPPI control strategies, considering the three predefined scenarios. For each scenario, two trials were conducted over the 25 individual forests, resulting in a total of 50 tasks ( $\mathcal{N}_T = 50$ ). In *Scenario #1*, where  $d_{\text{min}}^{\text{obs}} = 1.5\text{ m}$ , it is noteworthy that U-MPPI outperforms MPPI. Specifically, U-MPPI achieves a notably higher task completion percentage ( $\mathcal{T}_c = 98.78\%$ ) compared to MPPI ( $\mathcal{T}_c = 92.86\%$ ), effectively avoids collisions ( $\mathcal{N}_c = 0$ ), mitigates local minimum occurrences ( $\mathcal{R}_{\text{lm}} = 2$ ), and achieves a significantly higher success rate ( $\mathcal{S}_R = 96\%$  vs.  $\mathcal{S}_R = 78\%$  when MPPI is utilized). Furthermore, it successfully navigates the cluttered environment with a slightly improved average linear velocity  $v_{\text{av}}$ , which exhibits a very low standard deviation and approaches the maximum desired speed  $v_{\text{max}}$  of 2 m/s (likewise observed in the other two scenarios). Similarly, in *Scenario #2*, with a minimum obstacle distance of  $d_{\text{min}}^{\text{obs}} = 2\text{ m}$ , U-MPPI achieves a perfect task completion rate of 100%, outperforming MPPI's 98%, as it successfully avoids collisions and local minima, surpassing the baseline MPPI that experienced one collision with obstacles ( $\mathcal{N}_c = 1$ ) and encountered two instances of local minima ( $\mathcal{R}_{\text{lm}} = 2$ ).



In the least cluttered scenario, *Scenario #3*, both control strategies effectively complete all assigned tasks while successfully avoiding obstacles in the cluttered environment. However, U-MPPI stands out by offering a slightly more direct route towards the desired pose, with the robot traveling an average distance  $d_{av}$  of approximately 71.98 m, compared to 72.19 m when utilizing MPPI. On the contrary, in *Scenarios #1* and *#2*, MPPI demonstrates an enhanced performance in terms of the average distance traveled  $d_{av}$  by the robot when compared to our proposed U-MPPI. In the last column of Table I, despite both control methods ensuring *real-time* performance (since  $t_{exec.} < 33.33$  ms), it is worth emphasizing that the average execution time  $t_{exec.}$  of our proposed U-MPPI control strategy is slightly shorter than that of MPPI. This can be attributed to the parallel implementation of the U-MPPI algorithm on GPU, where each thread is responsible for computing the dynamics and costs of the entire batch when sampling from all sigma points ( $SM_1$ ). On the other hand, the parallel implementation of MPPI, as well as U-MPPI with sampling mode 0 ( $SM_0$ ), employs a single thread to compute each sampled trajectory, resulting in a relatively longer execution time, as evidenced by the intensive simulations in Table I, as well as Tasks #3 and #4 in Table II, where only the mean  $\mathcal{X}_k^{(0)}$  is used for trajectory sampling (i.e.,  $SM_0$ ).

To summarize, the intensive simulations clearly demonstrate that our U-MPPI method consistently outperforms the baseline MPPI control framework in all tested scenarios, particularly in environments with higher levels of clutter. These remarkable results can be credited to two key factors: the effective utilization of an unscented-based sampling strategy, which provides more flexible and efficient trajectories, and the incorporation of a *risk-sensitive* (RS) cost function that explicitly takes into account risk and uncertainty during the trajectory evaluation process; thanks to the incorporation of these crucial components, our approach ensures a significantly enhanced exploration of the state-space of the controlled system, even while leveraging the same injected Gaussian noise  $\delta \mathbf{u}_k$  into the mean control sequence, effectively reducing the likelihood of being trapped in local minima and yielding a safer and more resilient control system that is suitable for aggressive navigation in highly complex cluttered environments.

TABLE II: Influence of collision weighting coefficient  $w_{crash}$ , sampling mode (i.e.,  $SM_0$  &  $SM_1$ ), and UT parameters (namely,  $\Sigma_0, k_\sigma, \alpha$ ) on U-MPPI performance.

Test No.	$\mathcal{R}_{lm}(\mathcal{N}_c)$	$\mathcal{S}_R$ [%]	$\mathcal{T}_c$ [%]	$d_{av}$ [m]	$v_{av}$ [m/s]	$t_{exec.}$ [ms]
<b>Scenarios #1 and #2:</b> $w_{crash} = 500$ instead of $w_{crash} = 10^3$						
Test #1	2 (0)	96	99.4	74.43	$1.86 \pm 0.15$	8.69
Test #2	0 (0)	100	100	74.55	$2.56 \pm 0.56$	8.9
<b>Scenarios #1 and #2:</b> $SM_0$ instead of $SM_1$						
Test #3	3 (0)	94	98.24	75.88	$1.84 \pm 0.22$	12.87
Test #4	1 (0)	98	99.8	76.87	$2.47 \pm 0.67$	12.59
<b>Scenario #1:</b> Impact of UT parameters ( $\Sigma_0, k_\sigma, \alpha$ )						
Test #5	0 (0)	100	100	77.19	$1.79 \pm 0.23$	8.80
Test #6	1 (0)	98	98.7	74.65	$1.80 \pm 0.24$	8.88
Test #7	4 (0)	92	96.88	75.75	$1.81 \pm 0.25$	9.46
Test #8	9 (0)	82	92.91	75.25	$1.83 \pm 0.22$	9.02

To achieve a comprehensive understanding of how the behavior of the U-MPPI control strategy is affected by integrating the proposed sampling strategy and RS cost function, we expanded our intensive simulations in Table II to include varying operating conditions and hyper-parameters, differing from those utilized in Section V-A1. More precisely, in the first four intensive simulations (namely, Test #1 to Test #4), we investigate the potential benefits of integrating the RS cost function into the U-MPPI control strategy through two approaches: (i) reducing the collision weighting coefficient  $w_{crash}$  (specifically, Tests #1 and #2), and (ii) adopting sampling mode 0 ( $SM_0$ ) as an alternative to the default mode  $SM_1$  (i.e., Tests #3 and #4). Additionally, in the subsequent four tests, we extensively analyze the influence of the UT parameters on the performance of U-MPPI. For Tests #1 and #2, we replicated the U-MPPI simulations presented in Table I, specifically for *Scenarios #1* and *#2*, by assuming a reduced collision weighting coefficient  $w_{crash}$  of 500, representing half of its nominal value. We can clearly observe that lowering the value of  $w_{crash}$  has no significant impact on the success rate  $\mathcal{S}_R$  (as also depicted in Fig. 5(a)) and task completion rate  $\mathcal{T}_c$ . Nevertheless, it demonstrates improved performance in the robot's average travel distance  $d_{av}$  for completing the assigned tasks in both scenarios, outperforming both U-MPPI and MPPI as indicated in Table I. As an example, in *Scenario #2* shown in Fig. 5(b), we can observe that  $d_{av}$  is approximately 1.23 m shorter than that of U-MPPI when  $w_{crash}$  is set to  $10^3$ . On the contrary, we empirically observed that reducing  $w_{crash}$  in the case of MPPI, which utilizes a *risk-neutral* technique for evaluating sampled trajectories (as expressed in (17)), does not lead to a performance improvement, as depicted in Fig. 5(c). For instance, in *Scenario #1*, it can be noted from Fig. 5(c) that the success rate  $\mathcal{S}_R$  experiences a decline from 78% to 72% with the reduction of  $w_{crash}$ .

By employing sampling mode 0 ( $SM_0$ ) in Tests #3 and #4 as an alternative to the default sampling  $SM_1$  in U-MPPI, a slight decrease in performance is observed. However, U-MPPI continues to demonstrate impressive capabilities in successfully accomplishing assigned tasks and navigating around obstacles, outperforming the classical MPPI, particularly in *Scenario #1* (refer to Fig. 5(d)), owing to the integration of our efficient RS cost function for trajectory assessment. Furthermore, the comprehensive simulations performed in Tests #3 and #4 highlight the importance of employing the default sampling strategy  $SM_1$ , which takes into account all sigma points, in extremely challenging scenarios. This strategy leads to enhancements in both the success rate and the trajectory quality of the robot, as depicted in the illustrative example presented in Fig. 6(a). Now, it is time to delve into investigating how the key UT parameters (namely,  $\Sigma_0, k_\sigma, \alpha$ ) affect the distribution of sampled rollouts and their subsequent influence on the performance of the U-MPPI algorithm; to achieve this, we will explore their effects in highly cluttered environments, with a specific focus on *Scenario #1*. In Test #5, the initial state covariance matrix  $\Sigma_0$  is increased from  $0.001\mathbf{I}_3$  to  $0.005\mathbf{I}_3$ . It is observed that this increase in  $\Sigma_0$  results in a more conservative yet safer trajectory, with a success rate  $\mathcal{S}_R$  of 100% and an average traveled distance  $d_{av}$  of 77.19 m, compared to a success rate

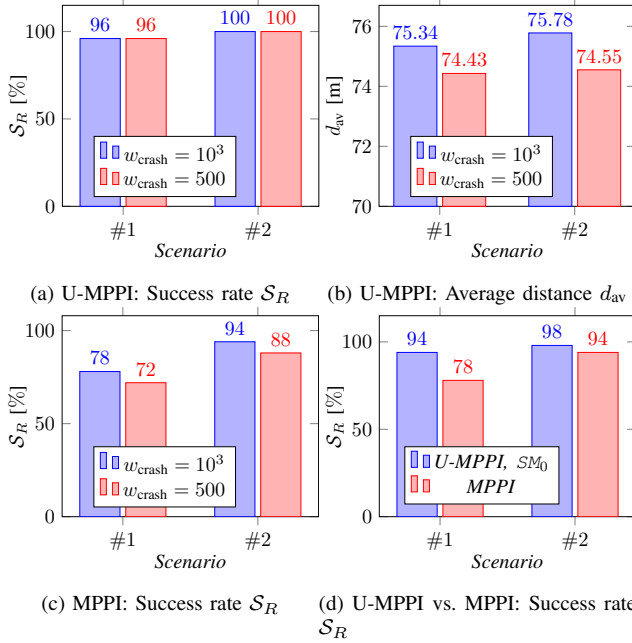
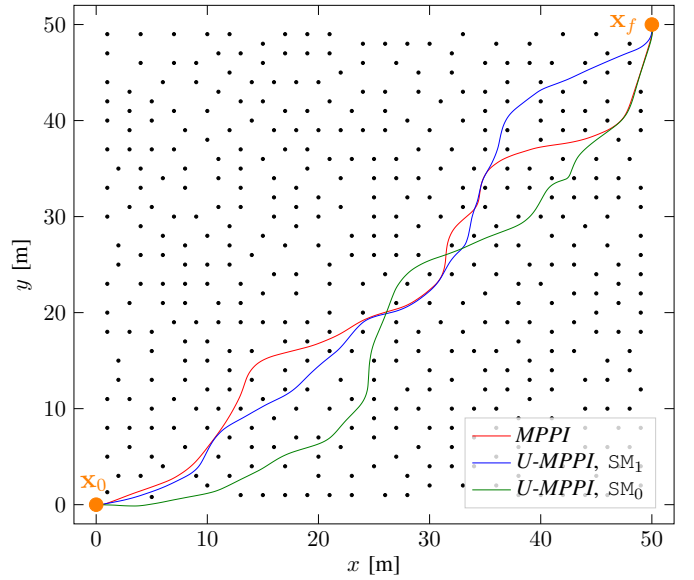


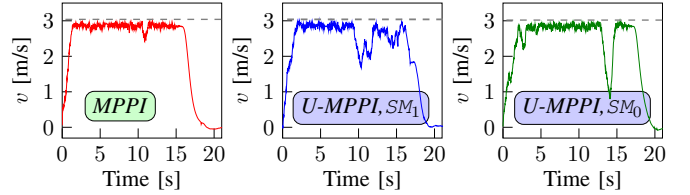
Fig. 5: Impact of decreasing collision weighting coefficient  $w_{\text{crash}}$  on (a) U-MPPI success rate  $S_R$ , (b) average distance traveled by the robot  $d_{\text{av}}$  in U-MPPI, and (c) MPPI success rate  $S_R$ , as well as (d) the effect of utilizing sampling mode 0 ( $SM_0$ ) on U-MPPI success rate  $S_R$  compared to MPPI success rate.

of 96% and an average distance of 75.34 m when  $\Sigma_0$  is set to  $0.001\mathbf{I}_3$ , as shown in Table I. During Tests #6 and #7, we adjust the UT scaling parameters ( $k_\sigma$  and  $\alpha$ ), which control the spread of sigma points; specifically, we increase  $k_\sigma$  from 0.5 to 3 in Test #6 and decrease  $\alpha$  from 1 to 0.1 in Test #7, while keeping all other parameters constant. It is noteworthy to observe in Test #6 that assigning a higher value to  $k_\sigma$ , along with  $\alpha = 1$ , generates more widely spread trajectories that cover a larger state space. This enables the robot to explore the environment more extensively and find better solutions, while improving the quality of the robot trajectory (as  $d_{\text{av}} = 74.65$  m), thereby reducing the likelihood of getting trapped in local minima. Conversely, reducing the spread of sigma points by assigning very low values to  $\alpha$  increases the likelihood of the robot becoming trapped in local minima, as illustrated in the simulations conducted during Test #7. In Test #8, we replicated the simulations from Test #7 using the same reduced UT scaling parameters ( $k_\sigma = 0.5$  and  $\alpha = 0.1$ ), while excluding the *risk-sensitive* behavior by setting the *risk-sensitive* parameter  $\gamma$  to 0, resulting in a constant penalty coefficients matrix  $Q_{\text{rs}}$  that is equal to the weighting matrix  $Q$ . Such a setup yields a sampling strategy closely resembling that of MPPI, resulting in the worst performance achieved, albeit only marginally better than the performance of MPPI illustrated in Table I.

In Fig. 6, we showcase the behavior of MPPI and U-MPPI (utilizing U-MPPI-specific sampling modes) in one of the randomly generated  $50\text{ m} \times 50\text{ m}$  cluttered environments with 2 m obstacles apart, i.e., *Scenario #2*. As shown in Fig. 6(a), both control strategies successfully achieve collision-free navigation in the cluttered environment. However, U-MPPI in the



(a) Robot trajectories comparison between MPPI and U-MPPI with random obstacles (black dots)



(b) MPPI: Robot velocity  $v$  (c) U-MPPI,  $SM_1$ :  $v$  (d) U-MPPI,  $SM_0$ :  $v$

Fig. 6: Performance analysis of MPPI and U-MPPI in a  $50\text{ m} \times 50\text{ m}$  cluttered environment with 2 m obstacle spacing (*Scenario #2*), utilizing U-MPPI-specific sampling modes ( $SM_0$  and  $SM_1$ ).

default sampling mode 1 ( $SM_1$ ) demonstrates a significantly shorter route to the desired pose, with a robot trajectory length  $d_{\text{av}}$  of 75.45 m, compared to 77.39 m for the classical MPPI and 78.33 m for U-MPPI in sampling mode 0 ( $SM_0$ ). In the given cluttered environment, as depicted in Fig. 6(b), MPPI demonstrates a smoother velocity profile compared to U-MPPI (see Figs. 6(c) and 6(d)), with an average traveling speed  $v_{\text{av}}$  of 2.63 m/s, as opposed to  $v_{\text{av}} = 2.52$  m/s for U-MPPI ( $SM_1$ ) and  $v_{\text{av}} = 2.57$  m/s for U-MPPI ( $SM_0$ ). Furthermore, it is worth noting that none of the control strategies violate the control (namely, velocity) constraint, which is defined as  $v \leq v_{\text{max}} = 3$  m/s, as observed from the velocity profiles.

## B. Aggressive Navigation in Unknown Environments

In Section V-A, although extensive simulations of our proposed control strategies are performed using the fully autonomous ClearPath Jackal robot to ensure their effectiveness and validate their performance in realistic scenarios, the autonomous navigation tasks in cluttered environments are typically carried out under the assumption that the costmap representing the environment is known beforehand. Such a setup or configuration could be limited in many real-world scenarios where autonomous robot systems often need to operate in *partially* observed environments due to the constraints of limited sensor range and the impracticality of obtaining

a complete map before task deployment [10]. To tackle this challenge, the robot needs to construct a *real-time* 2D local costmap, also known as a 2D occupancy grid map, centered at its current state; this grid map is utilized to store information about obstacles in the robot’s surrounding area, gathered from the incoming sensory data acquired by its on-board sensor. To this end, we utilize the *costmap\_2d* ROS package to generate the occupancy grid based on the sensory data, as depicted in Fig. 7(b) [29]. Afterward, the local costmap is incorporated into the optimization problem of the sampling-based MPC algorithm to assess sampled trajectories, aiming to achieve collision-free navigation. We refer to our previous work [16] and the corresponding open-source code<sup>2</sup>. In this work, we successfully integrated the 2D grid map into the MPPI algorithm.

1) *Simulation Setup*: We employ the same simulation setup for both control strategies previously presented in Section V-A1, with the exception that: (i) the collision indicator function  $q_{\text{crash}}(\mathbf{x})$  is herein calculated based on the robot-centered 2D grid map, and (ii) the time prediction is reduced to 6 s, resulting in  $N = 180$ , to be compatible with the size of the grid map. In this study, a 16-beam Velodyne LiDAR sensor mounted on the Clearpath Jackal AGV is used to construct the grid map (local costmap), with the costmap having dimensions of 240 cell  $\times$  240 cell and a resolution of 0.05 m/cell.

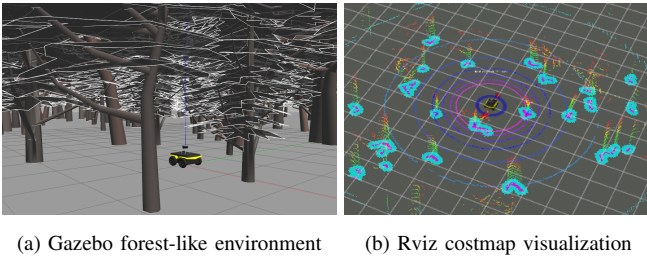


Fig. 7: Snapshot capturing (a) our Jackal robot operating in a forest-like environment, equipped with a Velodyne VLP-16 LiDAR sensor, and (b) the corresponding 2D local costmap generated by the on-board Velodyne LiDAR sensor, where purple and cyan cells depict obstacles and their inflation.

2) *Simulation Scenarios*: For the performance evaluation, we utilize two types of forest-like cluttered environments within the Gazebo simulator, each measuring 50m  $\times$  50m. The first type, referred to as *Forest #1*, consists of trees of different sizes with a density of 0.1 trees/m<sup>2</sup>, whereas the second type, known as *Forest #2*, contains tree-shaped obstacles with a density of 0.2 trees/m<sup>2</sup>. **In *Forest #1*, the maximum desired velocity  $v_{\text{max}}$  is 3 m/s, and the maximum desired angular velocity  $w_{\text{max}}$  is 3 rad/s. While in *Forest #2*, they are set to 2 m/s and 1 rad/s, respectively.**

3) *Performance Metrics*: To assess the efficiency of the U-MPPI control scheme in unknown environments, we compare it with the baseline MPPI by evaluating the predefined set of performance metrics outlined in Section V-A3, namely:  $\mathcal{R}_{\text{lm}}$ ,  $\mathcal{N}_c$ ,  $\mathcal{S}_R$ ,  $\mathcal{T}_c$ ,  $d_{\text{av}}$ ,  $v_{\text{av}}$ , and  $t_{\text{exec}}$ . In the first forest-like environment (*Forest #1*), the robot is directed to autonomously navigate from an initial pose  $G_0 = [0, 0, 0]^T$  to

a sequence of desired poses expressed in ([m], [m], [deg]):  $G_1 = [20, 20, 45]^T$ ,  $G_2 = [-18, 2, 0]^T$ ,  $G_3 = [20, -21, 90]^T$ ,  $G_4 = [20, 20, 0]^T$ , and ultimately reaching a stop at  $G_5 = [0, 0, 100]^T$ . Meanwhile, in *Forest #2*, for the sake of simplicity, the robot navigates solely from  $G_0$  to  $G_3$ , where it comes to a stop.

TABLE III: Performance statistics of the two control strategies over ten trials in *Forest #1* (0.1 trees/m<sup>2</sup>) and *Forest #2* (0.2 trees/m<sup>2</sup>).

Indicator	<i>Forest #1</i>		<i>Forest #2</i>	
	MPPI	U-MPPI	MPPI	U-MPPI
$\mathcal{R}_{\text{lm}}(\mathcal{N}_c)$	2 (0)	0 (0)	4 (1)	1 (0)
$\mathcal{S}_R$ [%]	80	100	50	90
$\mathcal{T}_c$ [%]	91.01	100	88.08	97.91
$d_{\text{av}}$ [m]	185.33 $\pm$ 0.43	185.37 $\pm$ 0.22	118.25 $\pm$ 1.7	116.76 $\pm$ 0.43
$v_{\text{av}}$ [m/s]	2.50 $\pm$ 0.68	2.40 $\pm$ 0.75	1.56 $\pm$ 0.44	1.67 $\pm$ 0.41
$t_{\text{exec}}$ [ms]	8.52 $\pm$ 0.61	9.87 $\pm$ 0.76	8.08 $\pm$ 0.91	10.75 $\pm$ 0.75

4) *Simulation Results*: In Table III, we present a comparison of performance statistics for the proposed control strategies in achieving goal-oriented autonomous navigation in both *Forest #1* and *Forest #2*, where the statistics are averaged over 10 trials for each environment. The obtained results validate the anticipated superiority of U-MPPI over MPPI in all scenarios, owing to its efficient unscented-based sampling distribution policy and *risk-sensitive* based trajectory evaluation technique. This superiority is evident in several aspects, including: (i) achieving a higher task completion rate  $\mathcal{T}_c$ , such as  $\mathcal{T}_c = 100\%$  with U-MPPI versus 91.01% when using MPPI in *Forest #1*, (ii) reducing the probability of encountering local minima, as demonstrated by the comparison in *Forest #2*, where U-MPPI leads to  $\mathcal{R}_{\text{lm}} = 1$  compared to  $\mathcal{R}_{\text{lm}} = 4$  with MPPI, and (iii) improving the quality of the generated robot trajectory, as evidenced by a significantly shorter average distance traveled by the robot  $d_{\text{av}}$ , particularly noticeable in *Forest #2*. Furthermore, it is worth emphasizing that both control methods guarantee *real-time* performance, highlighting the superiority of the sampling-based MPC algorithm, particularly our proposed U-MPPI, in incorporating not only the local costmap but also the unscented transform into the optimization problem without introducing additional complexity.

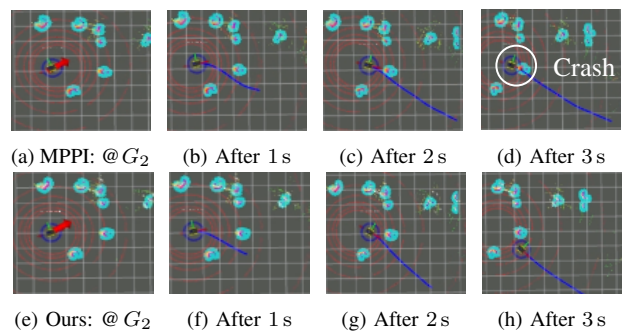


Fig. 8: Planned trajectories by MPPI (first row) and U-MPPI (second row) using the 2D local costmap, starting from the updated pose  $G_2 = [-18, 2, 40]^T$  and navigating towards  $G_3 = [20, -21, 90]^T$ .

To showcase the superior performance of U-MPPI compared to conventional MPPI in enhancing control safety during

<sup>2</sup>[https://github.com/IhlabMohamed/log-MPPI\\_ros](https://github.com/IhlabMohamed/log-MPPI_ros)

aggressive navigation, we introduce a specific adjustment to the  $G_2$  configuration within *Forest #1*. This adjustment entails shifting the desired heading angle from 0 to 40 degrees (see Fig. 8(a)), resulting in  $G_2 = [-18, 2, 40]^T$  instead of  $G_2 = [-18, 2, 0]^T$ , which in turn requires the robot to perform additional rotational maneuvers. Throughout five simulation runs, our proposed approach effectively completes all trials while penalizing trajectories with  $w_{\max}$  values exceeding 3 rad/s. Figures 8(e) to 8(h) depict snapshots of collision-free and predicted optimal trajectories generated by U-MPPI at three successive time points as the robot advances towards its target pose,  $G_3$ . On the other hand, when MPPI is employed, the robot experiences collisions with the same tree on three separate occasions out of the five trials, as depicted in Fig. 8(d). It is noteworthy that a lower value of  $w_{\max}$  is associated with improved MPPI performance. For instance, setting  $w_{\max}$  to 1 rad/s results in the successful completion of all trials without any collisions. These outcomes emphasize the enhanced safety delivered by our U-MPPI method without imposing excessive constraints on control inputs.

## VI. REAL-WORLD DEMONSTRATION

In this section, we conduct experiments to demonstrate the effectiveness and practicality of the proposed control strategies in achieving *real-time*, collision-free 2D navigation within an unknown and cluttered indoor environment.

1) *Experimental Setup and Validation Environment*: In our experimental configuration, we utilize an autonomous Clearpath Jackal robot equipped with a 16-beam Velodyne LiDAR sensor, which serves the purposes of generating the local costmap and estimating the robot's pose through the Lidar Odometry and Mapping (LOAM) algorithm [30]. Additionally, we employ the simulation setup previously outlined in Sections V-A1 and V-B1, with two specific modifications: (i) we adjust the maximum speed  $v_{\max}$  to 1.3 m/s to mitigate the robot localization error associated with using the Velodyne as a source of localization, and (ii) we extend the time prediction to 8 s, an increase from the 6 s duration specified in Section V-B1. We conduct experimental validation in an indoor corridor cluttered with randomly placed, varying-sized box-like obstacles, as depicted in Fig. 9.



Fig. 9: Snapshot of our Jackal robot equipped with a Velodyne VLP-16 LiDAR and located in an indoor unknown cluttered corridor environment.

In this setting, the robot's assigned control mission is to navigate from the following desired poses (in [m], [m], [deg]):  $G_1 = [0, 0, 0]^T$ ,  $G_2 = [26, 0.3, 170]^T$ , and then return to  $G_1$ .

2) *Performance Metrics*: We adhere to the predefined set of performance metrics detailed in Section V-A3. Furthermore,

given the significant uncertainties and noise inherent in real-world conditions (e.g., caused by LOAM) and the presence of unknown environmental factors, the robot's motion tends to be less smooth than in simulations. To facilitate a more thorough performance evaluation between the two proposed control methods, we opt to calculate the cumulative linear and angular jerks ( $J_{\text{acc}}, \zeta_{\text{acc}}$ ). Jerk, which represents the time derivative of acceleration, is linked to sudden changes in the forces exerted by the vehicle's actuators. Consequently, we can quantify the smoothness of the robot's velocity and steering by examining jerk as a metric [31]:

$$J_{\text{acc}} = \frac{1}{T_{\text{tot}}} \int_0^{T_{\text{tot}}} [\ddot{v}(t)]^2 dt, \quad (19)$$

$$\zeta_{\text{acc}} = \frac{1}{T_{\text{tot}}} \int_0^{T_{\text{tot}}} [\ddot{\omega}(t)]^2 dt, \quad (20)$$

where  $T_{\text{tot}}$  represents the complete duration required for the robot to execute its control mission. Additionally, we introduce the variable  $\mathcal{E}_{\text{loc}} = [\mathcal{E}_x, \mathcal{E}_y, \mathcal{E}_\theta]^T$ , which signifies the average drift or localization error in the robot's pose relative to the world frame  $\mathcal{F}_o$ , as displayed in Fig. 10.

TABLE IV: Performance statistics of the two control strategies over six trials in an indoor corridor environment.

Indicator	MPPI	U-MPPI
$\mathcal{R}_{\text{lm}}(\mathcal{N}_c)$	0 (1)	0 (0)
$d_{\text{av}}$ [m]	$56.58 \pm 0.33$	$56.01 \pm 0.46$
$v_{\text{av}}$ [m/s]	$1.01 \pm 0.32$	$1.02 \pm 0.28$
$t_{\text{exec.}}$ [ms]	$9.07 \pm 0.40$	$10.78 \pm 0.42$
$J_{\text{acc}}$ [ $\text{m}^2/\text{s}^3$ ]	$257.75 \pm 62.99$	$228.15 \pm 22.01$
$\zeta_{\text{acc}}$ [ $\text{rad}^2/\text{s}^3$ ]	$306.91 \pm 15.74$	$263.02 \pm 25.10$
$\mathcal{E}_x$ [m] w.r.t. $\mathcal{F}_o$	$0.38 \pm 0.67$	$0.10 \pm 0.28$
$\mathcal{E}_y$ [m] w.r.t. $\mathcal{F}_o$	$0.30 \pm 0.34$	$-0.04 \pm 0.04$
$\mathcal{E}_\theta$ [deg] w.r.t. $\mathcal{F}_o$	$7.20 \pm 11.65$	$0.80 \pm 3.71$

3) *Experimental Results*: The performance statistics comparison between the two control strategies, MPPI and U-MPPI, across six trials in our indoor corridor environment is summarized in Table IV. Throughout all trials, U-MPPI consistently outperforms MPPI in collision avoidance, ensuring collision-free navigation with zero collisions, whereas MPPI averages one collision. While both control strategies exhibit similar performance in terms of the average distance traveled  $d_{\text{av}}$  by the robot, average linear velocities  $v_{\text{av}}$ , and *real-time* performance guarantee (with  $t_{\text{exec.}} < 33.33$  ms), U-MPPI demonstrates a slightly longer average execution time per iteration  $t_{\text{exec.}}$  when compared to MPPI, due to its incorporation of both the local costmap and the unscented transform into the U-MPPI optimization problem. It is noteworthy to observe that U-MPPI showcases smoother motion, as indicated by lower cumulative linear jerk  $J_{\text{acc}}$  at  $228.15 \text{ m}^2/\text{s}^3$  and angular jerk  $\zeta_{\text{acc}}$  at  $263.02 \text{ rad}^2/\text{s}^3$ , whereas MPPI exhibits higher jerk values ( $257.75 \text{ m}^2/\text{s}^3$  and  $306.91 \text{ rad}^2/\text{s}^3$ , respectively). As a result of this enhanced motion smoothness, U-MPPI demonstrates improved robot localization accuracy based on LOAM, with smaller errors in both the  $x$ -direction ( $\mathcal{E}_x = 0.1$  m) and the  $y$ -direction ( $\mathcal{E}_y = -0.04$  m), relative to the reference frame  $\mathcal{F}_o$ , compared to MPPI (0.38 m and 0.30 m, respectively). However, MPPI has a slightly higher

orientation error, specifically  $\mathcal{E}_\theta = 7.20$  deg, compared to  $\mathcal{E}_\theta = 0.80$  deg when U-MPPI is utilized. Figure 10 depicts the accumulated robot pose estimation errors generated by LOAM after completing the control mission for the worst trial among the six conducted trials for both control strategies. Thanks to incorporating uncertainty information throughout the trajectory evaluation process, U-MPPI can avoid aggressive control sequences (motions) that may, in sequence, negatively impact LOAM localization accuracy. These findings emphasize the benefits of U-MPPI in terms of collision avoidance, motion smoothness, and localization accuracy, all while recognizing the trade-off of a slightly longer execution time. More details about both simulation and experimental results are included in this video: <https://youtu.be/1xsh4BxIrnq>.

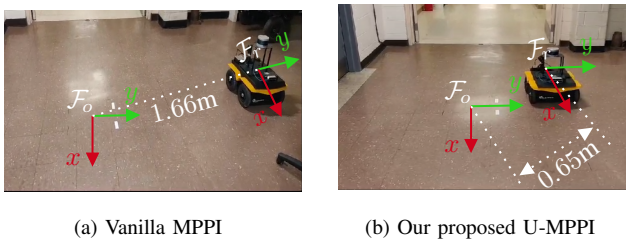


Fig. 10: Visualization of the cumulative errors in the robot's pose estimation generated by LOAM for the worst trial in the case of employing (a) MPPI and (b) U-MPPI.

## VII. CONCLUSION AND FUTURE WORK

In this paper, we proposed the U-MPPI control strategy, a novel methodology that enhances the vanilla MPPI algorithm by leveraging the unscented transform for two primary objectives. Firstly, it regulates the propagation of the dynamical system, resulting in a more effective sampling distribution policy that effectively propagates both the mean  $\bar{\mathbf{x}}_k$  and covariance  $\Sigma_k$  of the state vector  $\mathbf{x}_k$  at each time-step  $k$ . Secondly, it incorporates a *risk-sensitive* cost function that explicitly accounts for risk or uncertainty throughout the trajectory evaluation process. Through extensive simulations and real-world demonstrations, we demonstrated the effectiveness of U-MPPI in achieving aggressive collision-free navigation in both known and unknown cluttered environments. By comparing it to MPPI, our approach accomplished a substantial improvement in state-space exploration while utilizing the same injected Gaussian noise  $\delta\mathbf{u}_k$  in the mean control sequence. As a result, it yielded higher success and task completion rates, effectively minimizing the likelihood of getting trapped in local minima, and enabling the robot to identify feasible trajectories that avoid collisions. Our future plan involves incorporating chance constraints [4] into the U-MPPI control architecture to effectively address uncertainties in system dynamics and the environment, including moving obstacles, resulting in an enhanced safety and robustness of the control system to handle uncertain conditions, especially in safety-critical applications.

## REFERENCES

[1] H. Kurniawati, Y. Du, D. Hsu, and W. S. Lee, "Motion planning under uncertainty for robotic tasks with long time horizons," *The International Journal of Robotics Research*, vol. 30, no. 3, pp. 308–323, 2011.

[2] A. Bemporad and M. Morari, "Robust model predictive control: A survey," in *Robustness in identification and control*. Springer, 2007, pp. 207–226.

[3] A. Mesbah, "Stochastic model predictive control: An overview and perspectives for future research," *IEEE Control Systems Magazine*, vol. 36, no. 6, pp. 30–44, 2016.

[4] N. E. Du Toit and J. W. Burdick, "Probabilistic collision checking with chance constraints," *IEEE Transactions on Robotics*, vol. 27, no. 4, pp. 809–815, 2011.

[5] L. Hewing and M. N. Zeilinger, "Stochastic model predictive control for linear systems using probabilistic reachable sets," in *2018 IEEE Conference on Decision and Control (CDC)*. IEEE, 2018, pp. 5182–5188.

[6] S. A. Sajadi-Alamdari, H. Voos, and M. Darouach, "Risk-averse stochastic nonlinear model predictive control for real-time safety-critical systems," *IFAC-PapersOnLine*, vol. 50, no. 1, pp. 5991–5997, 2017.

[7] X. Yang and J. Maciejowski, "Risk-sensitive model predictive control with gaussian process models," *IFAC-PapersOnLine*, vol. 48, no. 28, pp. 374–379, 2015.

[8] E. Hyeon, Y. Kim, and A. G. Stefanopoulou, "Fast risk-sensitive model predictive control for systems with time-series forecasting uncertainties," in *2020 59th IEEE Conference on Decision and Control (CDC)*. IEEE, 2020, pp. 2515–2520.

[9] M. Schuurmans, A. Katriniok, H. E. Tseng, and P. Patrinos, "Learning-based risk-averse model predictive control for adaptive cruise control with stochastic driver models," *IFAC-PapersOnLine*, vol. 53, no. 2, pp. 15 128–15 133, 2020.

[10] I. S. Mohamed, G. Allibert, and P. Martinet, "Model predictive path integral control framework for partially observable navigation: A quadrotor case study," in *16th Int. Conf. on Control, Automation, Robotics and Vision (ICARCV)*, Shenzhen, China, Dec. 2020, pp. 196–203.

[11] G. Williams, A. Aldrich, and E. A. Theodorou, "Model predictive path integral control: From theory to parallel computation," *Journal of Guidance, Control, and Dynamics*, vol. 40, no. 2, pp. 344–357, 2017.

[12] I. S. Mohamed, G. Allibert, and P. Martinet, "Sampling-based MPC for constrained vision based control," in *IEEE/RSJ Int. Conf. on Intelligent Robots and Systems (IROS)*, 2021, pp. 3753–3758.

[13] J. Pravitra, K. A. Ackerman, C. Cao, N. Hovakimyan, and E. A. Theodorou, " $\mathcal{L}_1$ -adaptive MPPI architecture for robust and agile control of multirotors," in *IEEE/RSJ Int. Conf. on Intelligent Robots and Systems (IROS)*, 2020, pp. 7661–7666.

[14] I. S. Mohamed, "MPPI-VS: Sampling-based model predictive control strategy for constrained image-based and position-based visual servoing," *arXiv preprint arXiv:2104.04925*, 2021.

[15] J. Yin, Z. Zhang, E. Theodorou, and P. Tsiotras, "Trajectory distribution control for model predictive path integral control using covariance steering," in *IEEE Int. Conf. on Robotics and Automation (ICRA)*, 2022, pp. 1478–1484.

[16] I. S. Mohamed, K. Yin, and L. Liu, "Autonomous navigation of AGVs in unknown cluttered environments: log-MPPI control strategy," *IEEE Robotics and Automation Letters*, vol. 7, no. 4, pp. 10 240–10 247, 2022.

[17] G. Williams, B. Goldfain, P. Drews, K. Saigol, J. M. Rehg, and E. A. Theodorou, "Robust sampling based model predictive control with sparse objective information," in *Robotics: Science and Systems*, Pittsburgh, Pennsylvania, USA, 2018, pp. 42–51.

[18] J. Yin, Z. Zhang, and P. Tsiotras, "Risk-aware model predictive path integral control using conditional value-at-risk," *arXiv preprint arXiv:2209.12842*, 2022.

[19] I. M. Ross, R. J. Proulx, and M. Karpenko, "Unscented guidance," in *American Control Conference (ACC)*. IEEE, 2015, pp. 5605–5610.

[20] A. Savitzky and M. J. Golay, "Smoothing and differentiation of data by simplified least squares procedures," *Analytical chemistry*, vol. 36, no. 8, pp. 1627–1639, 1964.

[21] S. J. Julier, J. K. Uhlmann, and H. F. Durrant-Whyte, "A new approach for filtering nonlinear systems," in *Proceedings of 1995 American Control Conference-ACC'95*, vol. 3. IEEE, 1995, pp. 1628–1632.

[22] J. Xu, K. Yin, and L. Liu, "Online planning in uncertain and dynamic environment in the presence of multiple mobile vehicles," in *IEEE/RSJ International Conference on Intelligent Robots and Systems (IROS)*, 2020, pp. 2410–2416.

[23] R. Van Der Merwe, "Sigma-point kalman filters for probabilistic inference in dynamic state-space models," Ph.D. dissertation, Oregon Health & Science University, 2004.

[24] S. J. Julier, "The scaled unscented transformation," in *American Control Conference*, vol. 6. IEEE, 2002, pp. 4555–4559.

- [25] I. M. Ross, R. J. Proulx, and M. Karpenko, "Unscented optimal control for space flight," in *International Symposium on Space Flight Dynamics (ISSFD)*, 2014, pp. 1–12.
- [26] N. Ozaki, S. Campagnola, and R. Funase, "Tube stochastic optimal control for nonlinear constrained trajectory optimization problems," *Journal of Guidance, Control, and Dynamics*, 2020.
- [27] P. Whittle, "Risk-sensitive linear/quadratic/gaussian control," *Advances in Applied Probability*, vol. 13, no. 4, pp. 764–777, 1981.
- [28] G. Williams, P. Drews, B. Goldfain, J. M. Rehg, and E. A. Theodorou, "Information-theoretic model predictive control: Theory and applications to autonomous driving," *IEEE Transactions on Robotics*, vol. 34, no. 6, pp. 1603–1622, 2018.
- [29] E. Marder-Eppstein, D. V. Lu!!, and D. Hershberger. Costmap\_2d package. [Online]. Available: [http://wiki.ros.org/costmap\\_2d](http://wiki.ros.org/costmap_2d)
- [30] J. Zhang and S. Singh, "LOAM: Lidar odometry and mapping in real-time," in *Robotics: Science and Systems*, vol. 2, no. 9. Berkeley, CA, 2014, pp. 1–9.
- [31] M. Ali and L. Liu, "GP-frontier for local mapless navigation," in *IEEE International Conference on Robotics and Automation (ICRA)*, 2023, pp. 10 047–10 053.
- [32] M. A. Woodbury, *Inverting modified matrices*. Department of Statistics, Princeton University, 1950.

## APPENDIX A DERIVATIVE OF *Risk-Sensitive* COST

Considering the *risk-sensitive* cost defined as:

$$q_{rs}(\mathbf{x}_k) = -\frac{2}{\gamma} \log \mathbb{E} \left[ \exp \left( -\frac{1}{2} \gamma \|\mathbf{x}_k - \mathbf{x}_f\|_Q^2 \right) \right], \quad (21)$$

our objective is to obtain the following formulation:

$$q_{rs}(\mathbf{x}_k) = \frac{1}{\gamma} \log \det(\mathbf{I} + \gamma Q \boldsymbol{\Sigma}_k) + \|\bar{\mathbf{x}}_k - \mathbf{x}_f\|_{Q_{rs}}^2, \quad (22)$$

where  $Q_{rs} = (Q^{-1} + \gamma \boldsymbol{\Sigma}_k)^{-1}$ ,  $Q$  is a diagonal matrix, and  $\boldsymbol{\Sigma}_k$  is a symmetric matrix. We assume that the system state  $\mathbf{x}_k$  follows a Gaussian distribution  $\mathcal{N}(\bar{\mathbf{x}}_k, \boldsymbol{\Sigma}_k)$ , and  $\mathbf{x}_f$  represents the reference (desired) state. To derive the expression for  $q_{rs}(\mathbf{x}_k)$  as presented in (22), we will proceed with a step-by-step derivation as follows. We will start by expanding the quadratic form in (21):

$$\begin{aligned} q_{rs}(\mathbf{x}_k) &= -\frac{2}{\gamma} \log \mathbb{E} \left[ \exp \left\{ -\frac{\gamma}{2} \|\mathbf{x}_k - \mathbf{x}_f\|_Q^2 \right\} \right] \\ &= -\frac{2}{\gamma} \log \mathbb{E} \left[ \exp \left\{ -\frac{\gamma}{2} (\mathbf{x}_k - \mathbf{x}_f)^\top Q (\mathbf{x}_k - \mathbf{x}_f) \right\} \right]. \end{aligned} \quad (23)$$

Since  $\mathbf{x}_k \sim \mathcal{N}(\bar{\mathbf{x}}_k, \boldsymbol{\Sigma}_k)$ , we can assume that  $\mathbf{x}_k = \bar{\mathbf{x}}_k + \mathbf{e}_k$ , where  $\mathbf{e}_k \sim \mathcal{N}(0, \boldsymbol{\Sigma}_k)$ . Therefore, by substituting  $\mathbf{x}_k$  in (23), we can express the expectation as follows:

$$\begin{aligned} q_{rs} &= -\frac{2}{\gamma} \log \mathbb{E} \left[ \exp \left\{ -\frac{\gamma}{2} \bar{\mathbf{x}}_k^\top Q \bar{\mathbf{x}}_k - \gamma \mathbf{e}_k^\top Q \bar{\mathbf{x}}_k - \frac{\gamma}{2} \mathbf{e}_k^\top Q \mathbf{e}_k \right\} \right] \\ &= -\frac{2}{\gamma} \log \mathbb{E} \left[ \exp \left\{ -\frac{\gamma}{2} \bar{\mathbf{x}}_k^\top Q \bar{\mathbf{x}}_k \right\} \right. \\ &\quad \left. \times \exp \left\{ -\gamma \mathbf{e}_k^\top Q \bar{\mathbf{x}}_k - \frac{\gamma}{2} \mathbf{e}_k^\top Q \mathbf{e}_k \right\} \right] \\ &= \|\bar{\mathbf{x}}_k\|_Q^2 - \frac{2}{\gamma} \log \mathbb{E} \left[ \exp \left\{ -\frac{\gamma}{2} \|\mathbf{e}_k\|_Q^2 - \gamma \mathbf{e}_k^\top Q \bar{\mathbf{x}}_k \right\} \right], \end{aligned} \quad (24)$$

where  $\bar{\mathbf{x}}_k = \bar{\mathbf{x}}_k - \mathbf{x}_f$ . Now, to compute the expectation  $\mathbb{E}[\cdot]$  in (24), given by

$$-\frac{2}{\gamma} \log \mathbb{E} \left[ \exp \left\{ -\frac{\gamma}{2} \mathbf{e}_k^\top Q \mathbf{e}_k - \gamma \mathbf{e}_k^\top Q \bar{\mathbf{x}}_k \right\} \right], \quad (25)$$

we introduce a new term  $\mathbf{y}_k$  to simplify and express the expectation in the quadratic form. To achieve this, let us define  $\mathbf{y}_k = -\gamma \mathbf{K}^{-1} Q \bar{\mathbf{x}}_k$ , where  $\mathbf{K} = \gamma Q + \boldsymbol{\Sigma}_k^{-1}$ . By using this definition, we can accordingly prove that

$$\begin{aligned} &\frac{1}{2} (\mathbf{e}_k - \mathbf{y}_k)^\top \mathbf{K} (\mathbf{e}_k - \mathbf{y}_k) - \frac{1}{2} \mathbf{y}_k^\top \mathbf{K} \mathbf{y}_k \\ &= \frac{\gamma}{2} \mathbf{e}_k^\top Q \mathbf{e}_k + \frac{1}{2} \mathbf{e}_k^\top \boldsymbol{\Sigma}_k^{-1} \mathbf{e}_k + \gamma \mathbf{e}_k^\top Q \bar{\mathbf{x}}_k. \end{aligned} \quad (26)$$

Building on the equivalence in (26), we can approximate the expectation in (25) by integrating with respect to the distribution of the random variable  $\mathbf{e}_k$ . Since  $\mathbf{e}_k \sim \mathcal{N}(0, \boldsymbol{\Sigma}_k)$ , we can express it as follows:

$$\begin{aligned} &-\frac{2}{\gamma} \log \mathbb{E} \left[ \exp \left\{ -\frac{\gamma}{2} \mathbf{e}_k^\top Q \mathbf{e}_k - \gamma \mathbf{e}_k^\top Q \bar{\mathbf{x}}_k \right\} \right] \\ &= -\frac{2}{\gamma} \log \left( \int_{\mathbb{R}^n} \exp \left\{ \frac{-1}{2} (\mathbf{e}_k - \mathbf{y}_k)^\top \mathbf{K} (\mathbf{e}_k - \mathbf{y}_k) \right. \right. \\ &\quad \left. \left. + \frac{1}{2} \mathbf{y}_k^\top \mathbf{K} \mathbf{y}_k + \frac{1}{2} \mathbf{e}_k^\top \boldsymbol{\Sigma}_k^{-1} \mathbf{e}_k \right\} p(\mathbf{e}_k) d\mathbf{e}_k \right), \end{aligned} \quad (27)$$

where  $p(\mathbf{e}_k) = \frac{1}{\sqrt{\mathbf{A}}} \exp \left\{ -\frac{1}{2} \mathbf{e}_k^\top \boldsymbol{\Sigma}_k^{-1} \mathbf{e}_k \right\}$  represents the probability density function of  $\mathbf{e}_k$ . By substituting  $p(\mathbf{e}_k)$  in (27) and simplifying it further, we obtain:

$$\begin{aligned} &-\frac{2}{\gamma} \log \mathbb{E} \left[ \exp \left\{ -\frac{\gamma}{2} \mathbf{e}_k^\top Q \mathbf{e}_k - \gamma \mathbf{e}_k^\top Q \bar{\mathbf{x}}_k \right\} \right] \\ &= -\frac{2}{\gamma} \log \left( \frac{1}{\sqrt{\mathbf{A}}} \int_{\mathbb{R}^n} \exp \left\{ -\frac{1}{2} (\mathbf{e}_k - \mathbf{y}_k)^\top \mathbf{K} (\mathbf{e}_k - \mathbf{y}_k) \right. \right. \\ &\quad \left. \left. + \frac{1}{2} \mathbf{y}_k^\top \mathbf{K} \mathbf{y}_k \right\} d\mathbf{e}_k \right) \\ &= -\frac{2}{\gamma} \log \left( \frac{1}{\sqrt{\mathbf{A}}} \exp \left( \frac{1}{2} \mathbf{y}_k^\top \mathbf{K} \mathbf{y}_k \right) \right. \\ &\quad \left. \times \int_{\mathbb{R}^n} \exp \left\{ \frac{-1}{2} (\mathbf{e}_k - \mathbf{y}_k)^\top \mathbf{K} (\mathbf{e}_k - \mathbf{y}_k) \right\} d\mathbf{e}_k \right), \end{aligned} \quad (28)$$

where  $\mathbf{A} = (2\pi)^n \det \boldsymbol{\Sigma}_k$ . We can now evaluate the integral. Since the integrand is a Gaussian distribution with mean  $\mathbf{y}_k$  and covariance matrix  $\mathbf{K}^{-1}$ , the integral evaluates to  $\sqrt{\frac{(2\pi)^n}{\det \mathbf{K}}}$ . Substituting this back into the expression given in (28), we have:

$$\begin{aligned} &-\frac{2}{\gamma} \log \mathbb{E} \left[ \exp \left\{ -\frac{\gamma}{2} \mathbf{e}_k^\top Q \mathbf{e}_k - \gamma \mathbf{e}_k^\top Q \bar{\mathbf{x}}_k \right\} \right] \\ &= -\frac{2}{\gamma} \log \left( \frac{\exp \left( \frac{1}{2} \mathbf{y}_k^\top \mathbf{K} \mathbf{y}_k \right)}{\sqrt{(2\pi)^n \det \boldsymbol{\Sigma}_k}} \sqrt{\frac{(2\pi)^n}{\det \mathbf{K}}} \right) \\ &= -\frac{2}{\gamma} \log \left( \frac{\exp \left( \frac{1}{2} \mathbf{y}_k^\top \mathbf{K} \mathbf{y}_k \right)}{\sqrt{\det(\boldsymbol{\Sigma}_k \mathbf{K})}} \right) \\ &= \frac{1}{\gamma} \log \det(\boldsymbol{\Sigma}_k \mathbf{K}) - \frac{1}{\gamma} \mathbf{y}_k^\top \mathbf{K} \mathbf{y}_k \\ &= \frac{1}{\gamma} \log \det(\mathbf{I} + \gamma Q \boldsymbol{\Sigma}_k) - \frac{1}{\gamma} \mathbf{y}_k^\top \mathbf{K} \mathbf{y}_k. \end{aligned} \quad (29)$$

By substituting  $\mathbf{y}_k = -\gamma \mathbf{K}^{-1} Q \bar{\mathbf{x}}_k$ , and  $\mathbf{K} = \gamma Q + \boldsymbol{\Sigma}_k^{-1}$  into (29), we can simplify the second term  $-\frac{1}{\gamma} \mathbf{y}_k^\top \mathbf{K} \mathbf{y}_k$  as follows:

$$-\frac{1}{\gamma} \mathbf{y}_k^\top \mathbf{K} \mathbf{y}_k = -\gamma \bar{\mathbf{x}}_k^\top Q (\gamma Q + \boldsymbol{\Sigma}_k^{-1})^{-1} Q \bar{\mathbf{x}}_k, \quad (30)$$

assuming that  $Q$  is a diagonal matrix and  $\Sigma_k$  is a symmetric matrix. Afterward, we can utilize the Woodbury matrix identity to simplify the expression  $(\gamma Q + \Sigma_k^{-1})^{-1}$ , where the Woodbury matrix identity is defined as [32]:

$$(A + UCV)^{-1} = A^{-1} - A^{-1}U(C^{-1} + VA^{-1}U)^{-1}VA^{-1}. \quad (31)$$

By applying the Woodbury identity expressed in (31) to the given expression with  $A = \gamma Q$ ,  $C = \Sigma_k^{-1}$ , and  $U = V = \mathbf{I}$  (where  $\mathbf{I}$  denotes the identity matrix), we can rewrite  $(\gamma Q + \Sigma_k^{-1})^{-1}$  as follows:

$$(\gamma Q + \Sigma_k^{-1})^{-1} = \frac{1}{\gamma} Q^{-1} [\mathbf{I} - Q_{\text{rs}} Q^{-1}], \quad (32)$$

where  $Q_{\text{rs}} = (Q^{-1} + \gamma \Sigma_k)^{-1}$ . By substituting (32) back into (30), we obtain:

$$-\frac{1}{\gamma} \mathbf{y}_k^\top \mathbf{K} \mathbf{y}_k = -\|\bar{\mathbf{X}}_k\|_Q^2 + \|\bar{\mathbf{X}}_k\|_{Q_{\text{rs}}}^2. \quad (33)$$

Subsequently, by substituting (33) into (29) and further substituting the obtained results into (24), while replacing  $\bar{\mathbf{X}}_k$  with  $\bar{\mathbf{x}}_k - \mathbf{x}_f$ , the desired result can be obtained as follows:

$$q_{\text{rs}}(\mathbf{x}_k) = \frac{1}{\gamma} \log \det (\mathbf{I} + \gamma Q \Sigma_k) + \|\bar{\mathbf{x}}_k - \mathbf{x}_f\|_{Q_{\text{rs}}}^2. \quad (34)$$

It is worth emphasizing that a similar form of (34), along with its derivation, can be found in [8]. However, the presented derivation process in [8] is brief and lacks detailed explanations and clarifications.